CZECH TECHNICAL UNIVERSITY IN PRAGUE

Faculty of Nuclear Sciences and Physical Engineering

Department of Physics

Bachelor thesis

Jet production in heavy-ion collisions

Kateřina Moudrá

Supervisor: RNDr. Jana Bielčíková, Ph.D.

Prague, 2013

ČESKÉ VYSOKÉ UČENÍ TECHNICKÉ
V PRAZE
Fakulta Jaderná a Fyzikálně Inženýrská
Katedra Fyziky

Bakalářská práce

Produkce jetů v jádro-jaderných srážkách

Kateřina Moudrá

Supervisor: RNDr. Jana Bielčíková, Ph.D.

Praha, 2013

Prohlášení:

Prohlašuji, že jsem svou bakalářskou práci vypracoval samostatně a použil jsem pouze podklady (literaturu, software, atd.) uvedené v přiloženém seznamu.

Nemám závažný důvod proti užití tohoto školního díla ve smyslu 60 Zákona .121/2000 Sb., o právu autorském, o právech souvisejících s právem autorským a o změně některých zákonů (autorský zákon).

V Praze dne

Title:
Jet production in heavy-ion collisions

Author: Kateřina Moudrá

Specialization: Experimental nuclear physics

Sort of project: Bachelor thesis

Supervisor: RNDr. Jana Bielčíková, Ph.D.

Abstract: Nucleus-nucleus collisions enable to study the nuclear matter under extreme conditions. Jets are an important probe of the matter created in the early stage of such collision. Jet modifications are considered as one of the most promising indirect observables of quark gluon plasma, extremely hot and dense matter, which characterictics are not very well known in the present days. The aim of this thesis is to summarize the recent discoveries and experimental capabilities, describe important jet characteristics and provide an overview of various jet algorithms. This thesis also focuses on exploring the jet structure, with further insight to topological reconstruction of strange particles in jets. The work in this thesis is a preparation for further analysis of jet structure.

Key words: jet reconstruction, ALICE, quark-gluon plasma, heavy-ion collisions, topological reconstruction of strange particles

Název práce:
Produkce jetů v jádro-jaderných srážkách

Autor: Kateřina Moudrá

Abstrakt: Jádro-jaderné srážky umožňují studium jaderné hmoty za extrémních podmínek. Jety jsou důležitou sondou hmoty vytvořené v rané fázi srážky. Modifikace jetů je jedním z nejdůležitějších nepřímo pozorovatelných projevů kvark-gluonového plazmatu, extrémně horké a husté jaderné hmoty, jejíž vlastnosti nejsou v dnešní době dokonale probádány. Cílem této práce je shrnutí současných výsledků a experimentálních možností, popis důležitých vlastností jetů a poskytnutí přehledu algoritmů vyhledávajících jety. Tato práce se také zabývá zkoumáním struktury jetů se zaměřením na topologickou rekonstrukci podivných částic v jetech. Analýza v této práci je přípravou na budoucí analýzu struktury jetů.
Klíčová slova: rekonstrukce jetů, ALICE, kvark-gluonové plazma, jádro-jaderné srážky, topologická rekonstrukce podivných částic

Acknowledgement

I would like to express my gratitude to all who supported me and gave me an opportunity to complete this thesis. I am very grateful to my supervisor Jana Bielčíková, for her willingness, patience, professional feedback, language corrections and help with programming. I would also like to thank Vít Kučera for providing me the data for analysis and for being ready to help when I needed it.

Contents

List of Figures

List of Tables

Chapter 1

Particle physics and quark-gluon plasma

1.1 Standard model

Since ancient times, people longed to understand how the basic structure of matter looks like and how it was created. Standard model is a theory summarizing knowledge about known particles and electromagnetic, strong and weak interaction. The theory, however, is not complete, but gives us sucessfull reliable predictions.

According to this model, there are two main classes of fundamental particles:

- Leptons and quarks that are constituents of matter. They are fermions and obey Pauli principle.
- Gauge bosons, that mediate interactions. They do not obey Pauli principle.

Leptons and quarks

There are two types of fermions, quarks and leptons, which can be grupped in three generations. Each of these generations is repeating of the same structure but with different masses. The mass rises with number of generation. The first generation contains electron, electron neutrino and up and down quarks. The second generation contains muon, muon neutrino and strange and charm quarks. The third generation contains tauon, tau neutrino and top and bottom quarks. The overview of all generations can be seen at Figure 1.1.

Hadrons is a name of variety of particles formed by quarks. Hadrons made of three quarks are refered to as baryons, while hadrons made of two quarks are called mesons. As fermions have to obey Pauli principle, to explain the observed existence of hadrons consisting of the same quark flavor, as uuu, a new degree of freedom had to be declared. This degree of freedom is called color. Conventionally, each quark can have either red, green, or blue color (or specific anticolor) and all hadrons are color neutral. It has been shown [2], that in an ordinary hadronic matter, most particles are built from quarks from the

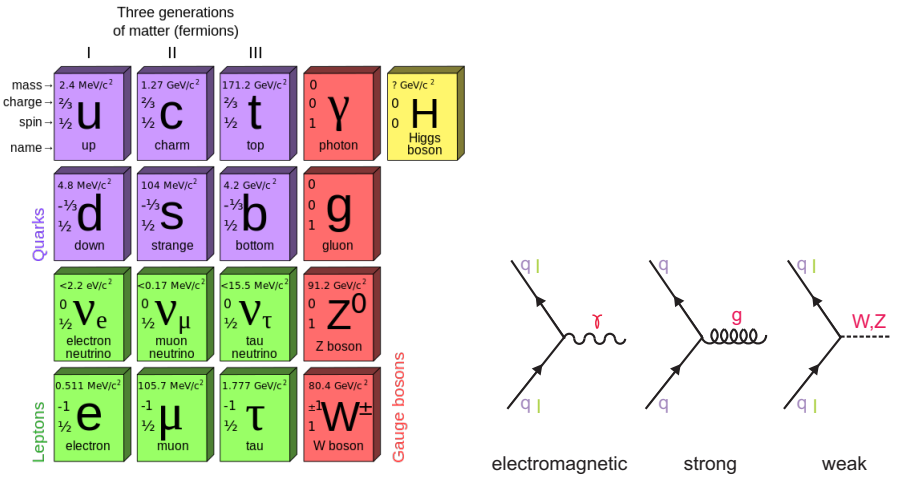

Figure 1.1: Left: Standard model. Three generations of quarks and leptons. Gauge bosons. Predicted Higgs boson. Taken from [1]. Right: Corresponding fundamental interactions.

Interaction	Gauge boson	Range	Relative force
Electromagnetic	Photon γ	∞	10^{-2}
Weak	Intermediate bosons W^{+-}, Z	$10^{-18}m$	10^{-7}
Strong	Quark q	$10^{-15}m$	1
Gravitational	Graviton G (not observed yet)	∞	10^{-39}

Table 1.1: An overview of four fundamental interactions, their gauge bosons, range and relative force with respect to strong interaction [3].

first generation – up and down quarks. Quarks from higher generation and hadrons made from them decay often quickly.

Gauge bosons

Gauge bosons are particles that mediate interactions. The standard model assumes three fundamental interactions, namely electromagnetic, weak and strong (see Figure 1.1). These interactions are described by a specific Quantum Field Theory (QFT). In quantum field theories, forces are mediated by specific gauge bosons. (The boson mediating gravitational interaction, graviton, has not been observed yet.)

The relative strength of an interaction is classified by a running coupling constant α, which depends on used momentum scale.The overview of forces and their gauge bosons and corresponding theories can be seen in Table 1.1.

A special role in the standard model is played by Higgs boson, which is supposed to give masses to all fermions and bosons. Search for Higgs boson is a part of the effort of todays science.

This thesis is primarily about effect of strong force, which is described by quantum chromodynamics, that will be briefly discussed in the next section.

1.2 Quantum chromodynamics

The theory, that describes strong force, is called QCD (Quantum ChromoDynamics). This theory has many similarities with QED (Quantum ElectroDynamics), which describes electromagnetic force. Whereas there is a single charge for electromagnetic force – electric charge, the charge of strong force is color charge, and exists in three varieties – red, green and blue (and corresponding anti-color charges). Both theories predict existence of a gauge boson as a carrier of the force. Like photon mediates electric charge, color charge is mediated by gluons. However, there is one crucial difference between QCD and QED. Unlike photon, which is electrically neutral, gluons themselves carry a color and so can self-interact, via the so called gluon self-coupling. This causes two following important characteristics of quark-gluon dynamics, which are schematically depicted in Figure1.2: [4]

- Quark confinement – At small distances and low energies, α rapidly rises. At these conditions, quarks are confined in hadrons. It is impossible to observe one free separated quark.
- Asympotic freedom – At high temperatures and high energy density, α tends to zero. If the temperature is extremely high, quarks and gluons might be able to move freely, which is called deconfinement.

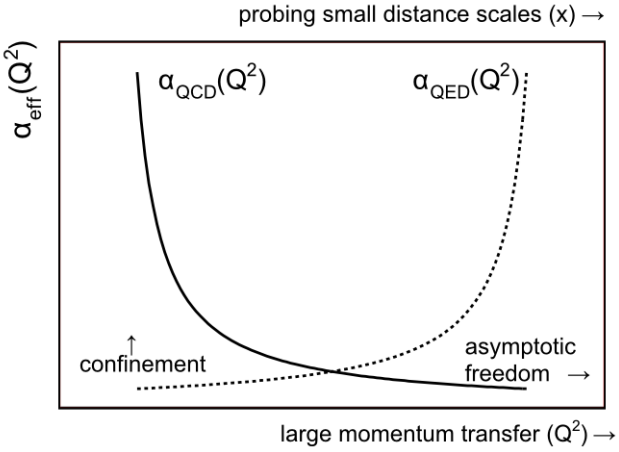

Figure 1.2: Behaviour of running coupling constants in QED and QCD. The variable Q represents transfered momentum and is proportional to the energy of a system. Taken from [5].

1.3 Quark-gluon plasma

The, by asymptotic freedom concept theoretically predicted, hot and dense state of matter where quarks and gluons are deconfined is called quark gluon plasma (QGP). The details about its dynamics, as well as details about its possible

phase transitions are not very well known in present days. They are theoretically difficult to describe and experimentally difficult to observe.

Figure 1.3 shows the predicted phase diagram of strongly interacting matter in the plane of temperature T vs baryon chemical potential μ_B. Particularly, the baryon chemical potential has a simmilar meaning as density.

Since we cross the deconfinement line, the hadronic matter transits to QGP. So, QGP can be reached either by increasing temperature, or by increasing baryon chemical potential.

Next to the critical point, the crossover region starts. Here the matter is predicted to transform to QGP in a rapid continuously way (thermodynamic quantities change smoothly) and not by a phase transition.

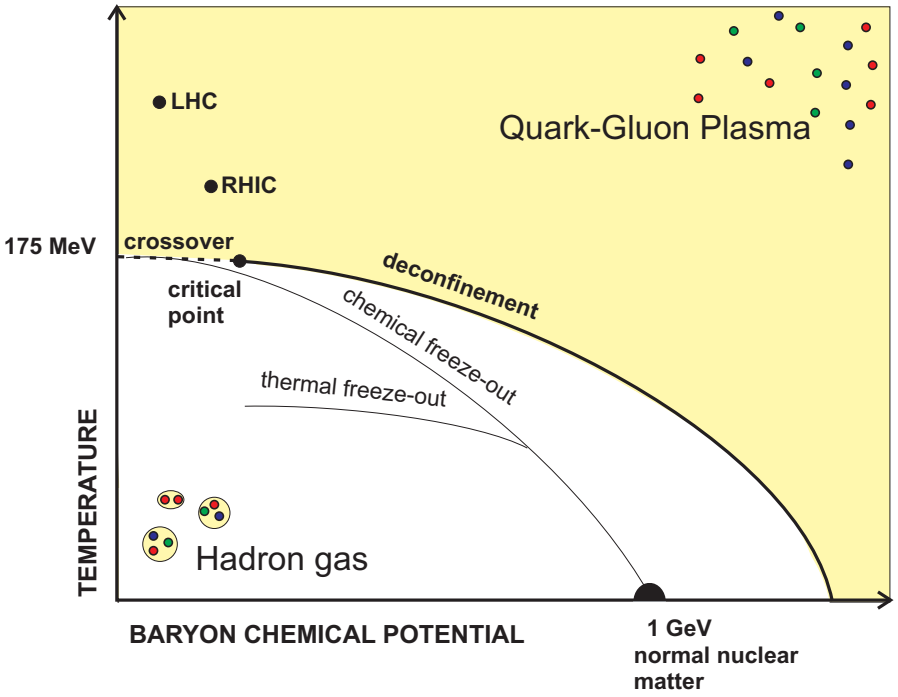

Figure 1.3: The predicted phase diagram of strongly interacting matter. The deconfinement line separates the confined hadronic matter and deconfined quark gluon plasma state. The chemical and thermal freeze out are defined in the next chapter.

It is believed, that the universe was created approximately 13.8 billion years ago through a process known as *Big bang*. A few microseconds after the Big Bang, the universe is expected to be in the extremely hot and dense QGP stage. Later, as the universe expanded and cooled, quarks and gluons turned to hadrons, which further formed atoms (See Figure 1.4). The research of quark-gluon plasma might explain characteristic of our universe and so give us information, why our universe developed the way it did.

The extreme conditions for creating of droplets of quark-gluon plasma, can

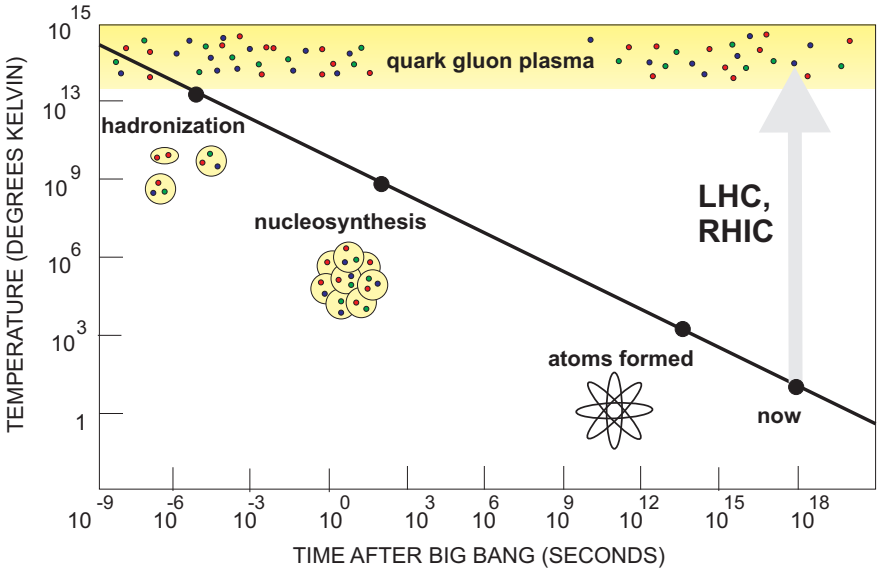

Figure 1.4: History of the universe. Formation of matter from QGP.

be reached in laboratory, namely in high energy nucleus-nucleus collisions. The regions in the phase diagram reached by RHIC and LHC experiments (see Chapter 6) are schematically displayed in Figure 1.3. It seems, that the best way to observe and study the early universe might be not by building a telescope, but by building a particle accelerator. In fact, this idea connects high energy physics and astrophysics, or, in other words, the smallest, and the largest measurable scales.

Chapter 2

Nucleus-nucleus collisions

In this chapter, basic characteristics of a nucleus-nucleus collision, namely geometry and space time evolution, will be discussed. Kinematical and dynamical variables of a collision can be found in Appendix A.

2.1 Geometry of a collision

Accelerated heavy nuclei in a collision experiment are, as a result of the relativistic effects, Lorentz contracted in the beam direction. They come to a collision as thin discs. During the collision, they can overlap with each other fully, or partially, or they can miss each other.

To describe the overlap region, centrality of a collision is defined. It is classified according to distance between center of colliding nuclei, namely impact parameter b [4], which is shown in Figure 2.1. If the impact parameter is close to 2R, where R is the radius of the nuclei, the nuclei only slightly touch each other and the collision is called ultra-peripheral collision. As the impact parameter decreases, the size of overlap region increases, and the collision is called peripheral collision. If the impact parameter is close to 0, the nuclei overlap with each other (they hit head on) and the collision is called central collision.

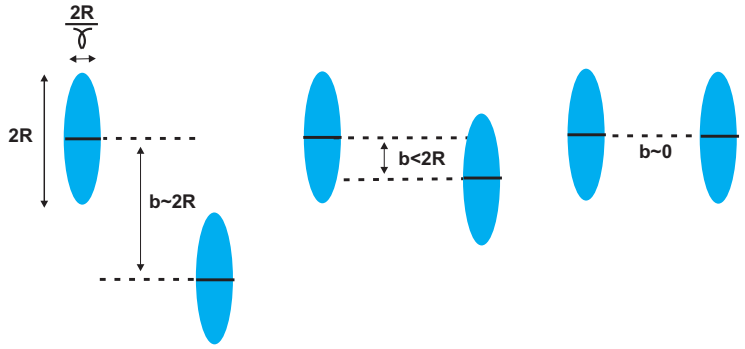

Figure 2.1: Centrality of a collision classified according to an impact parameter b. From left: ultra peripheral collision, peripheral collision, central collision.

The schematic view of a collision geometry is ilustrated at Figure 2.2. Nucleons, that are situated in the overlap region, suffer at least one binary collision ($N_{binary} \geq 1$, see Appendix B), and so participate in the collision are referred to as *participants*. The non interacting nucleons are referred to as *spectators*. After a collision, spectators continue moving in the beam direction, and often form unstable nuclei, which decay, while participants stay in the collision region and form a hot and dense medium, often referred to as *fireball*. If the medium is hot and dense enough, it can transform to QGP[4]. The interesting region in a collision for this thesis is the region of participants.

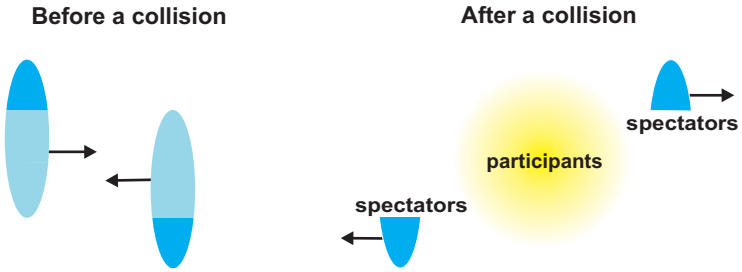

Figure 2.2: Participants and spectators before and after a collision. The yellow region is commonly referred to as *fireball*.

The number of interacting nucleons in a nucleus-nucleus collision can be characterized by a Glauber model [6] (see Appendix B).

2.2 Space-time evolution of a collision

There are three main phases [4] of space–time evolution of a collision: thermalization, expansion and decoupling. The nature of these processes is still an open question. The space time evolution of a collision with and without reaching the QGP state is depicted in Figure 2.3.

Expressed in a proper time τ, s collision where QGP state is reached, evolves as follows:

$0 < \tau < \tau_0$

Immediately after the collision, partons in the overlap region of colliding nuclei rescatter each other (both inelastically and elastically [7]) and are significantly slowed down. Energy density is very high. With energy density high enough, deconfined quarks and gluons are produced. The time of this stage is predicted to be about $\tau_0 = 1\text{fm}/c$ [4].

τ_0

The system reaches thermal equilibrium [4].

$\tau_0 < \tau < \tau_c$

High pressure of a system leads to expansion, which causes its cooling. Energy density decreases [4].

τ_c

At τ_c (*chemical freeze out time*) hadronization starts. Deconfinement is no longer possible and quarks and gluons are being converted again to hadrons. Inelastic scattering stops. This process is referred to as *chemical freeze out* [7].

$\tau_c < \tau < \tau_f$

Hadrons interact with each other. Expansion continues, primarily along the incident beam axis. Distances between hadrons increase, until the range of strong interaction is exceeded. At τ_f (*kinetic (thermal) freeze out time*) elastic scattering stops. This process is referred to as *kinetic (thermal) freeze out*[7].

τ_f

Decoupling starts. Hadrons are separated and do not interact strongly. In their final state, they freely stream out from the collision region and can be recorded by detectors [4].

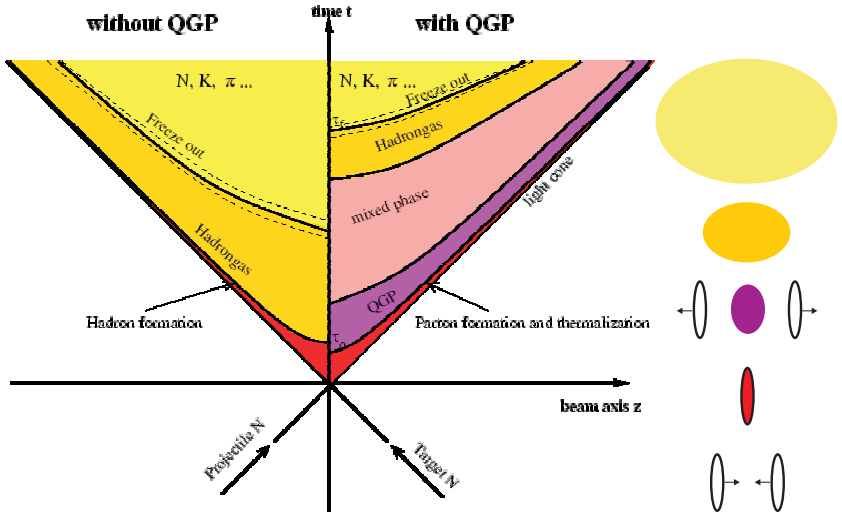

Figure 2.3: Left: Spacetime evolution of a collision with and without presence of QGP. Taken from [8]. Right: Corresponding schema of two colliding nuclei along the beam line.

Chapter 3

QGP in nucleus-nucleus collisions and recent results

As the QGP occurs only in the early stage of a collision, and immediately converts to hadronic matter, it cannot be directly observed. In detectors, hadrons in the final state are measured. There are several indirect observables considered as possible probes of presence of QGP. The most promising of them are enhancement of strangeness and charm, elliptic flow, quarkonia suppression, high transverse momentum (p_T, see Appendix A) suppression and jet quenching. Although this thesis is only about the last effect, which is associated with jets, all of them will be discussed briefly in the next paragraphs.

Enhanced production of strangeness and charm

In a quark gluon plasma, due to large energy density, up and down quarks occupy high energetic states. In that case it is energetically more favourable to create heavier quarks, namely the quarks from second generation- s and c. As a consequence, in contrast with normal hadronic matter formed by up and down quarks, significant increase of s and c quarks in heavy ion collisions containing QGP is expected. This increase was observed e.g. at STAR and ALICE experiments (see Figure 3.1).

Eliptic flow

After a collision, the particles are produced in a all directions. The azimuthal distribution of particle emission is experimentally, in terms of Fourier expansion, analyzed as follows:

$$E\frac{d^3N}{d^3p} = \frac{d^2N}{2\pi p_T dp_T dy}\left(1 + \sum 2v_n cos(n(\phi - \Phi_r))\right), \tag{3.1}$$

where p_T is the transverse momentum, y is rapidity, v_n is, ϕ is the azimuthal angle of the particle (see Appendix A), Φ_r is the azimuthal angle of the reaction plane in the laboratory frame [4].

In the system described by hydrodynamic laws, the emission pattern is affected by the shape of the system. In non central collisions, the overlapped region has an almond shape. The pressure gradient generates an eliptic flow

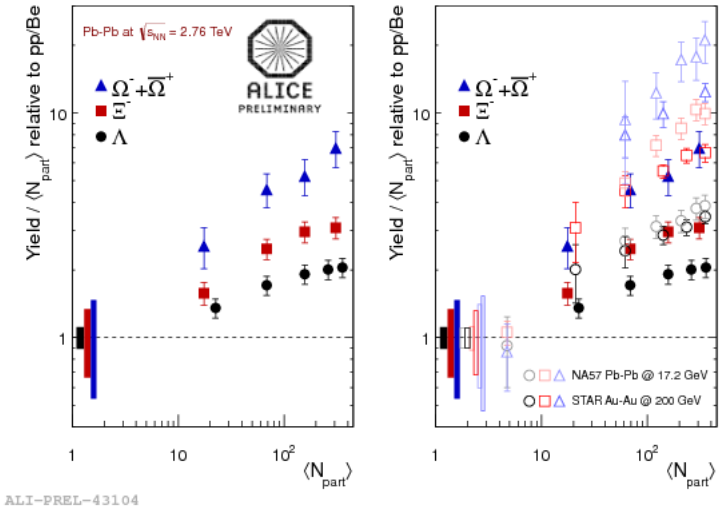

Figure 3.1: Left: Strangeness enhancement as a function of $\langle N_{part} \rangle$ for $\sqrt{s_{NN}} =$ 0.017, 0.2, and 2.76 TeV collisions relative to pBe (NA57) and pp (STAR, ALICE). Taken from [9].

(see Figure 3.2). Eliptic flow is represented by the second harmonics v_2 of the azimuthal particle distribution in Eq.(3.1) [4].

At RHIC eliptic flow measurements showed that the created matter equilibrates in an early stage of the collision and behaves like a perfect fluid, so its evolution can be described by the laws of the hydrodynamics. It has been shown, that in the ALICE experiment, in PbPb collisions at center of mass energy (see Appendix A) $\sqrt{s_{NN}} = 2.76$ TeV per nucleon pair, the eliptic flow increased by about 30 percent in comparison with the flow measured at RHIC at 0.2 TeV [10].

Enhancement of dileptons

Dilepton is a particle- antiparticle pair of the same flavour leptons. They can be created by interaction of quark- antiquark pair in the early stage of a collision. As they have no color charge, they interact only weakly with the QGP medium and can escape from the interaction region easily, than strong interacting quarks and hadrons. Therefore, dileptons can give us information about the medium directly from the early stage of the reaction zone [4].

Quarkonia supression

Quarkonia are mesons containing heavy quark (c,b) and antiquark of the same type. The presence of QGP, due to mechanism known as color-screening, leads to their suppression. Because each type of quarkonia is being suppressed at different temperature, as ilustrated at Figure 3.3, they can succesive be used as a "thermometer" of hot and dense matter. By this sequential melting of quarkonia, it can be determined if the critical temperature was exceeded and thereby predict the presence of QGP [4].

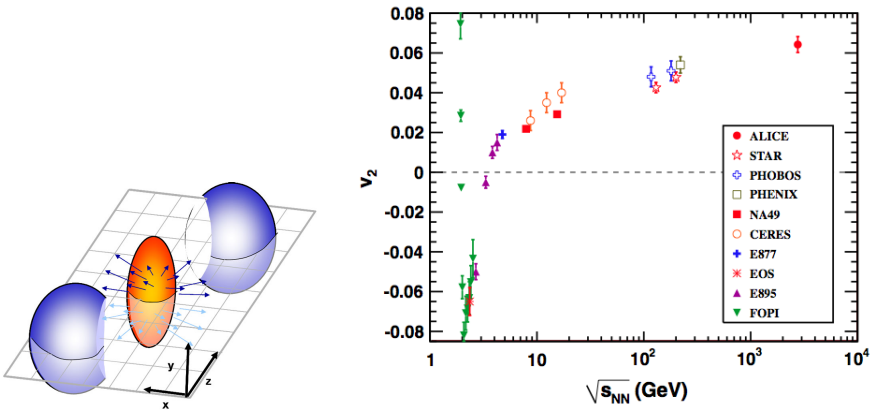

Figure 3.2: Left: A schema ilustrating eliptic flow generated by the pressure gradient. Taken from [11]. Right: Magnitude of eliptic flow v_2 (from Eq.(3.1)) from todays experiments, including STAR and ALICE. Taken from [10].

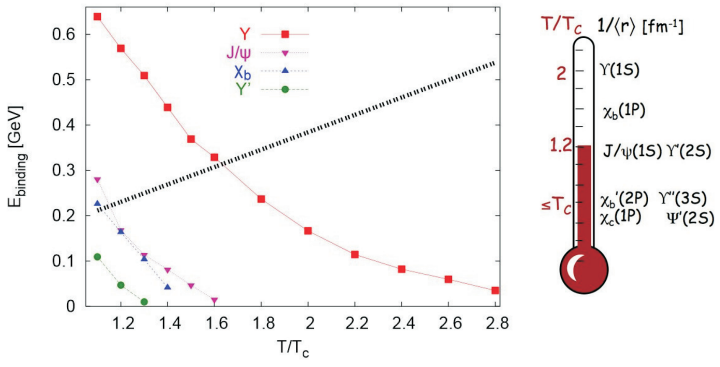

Figure 3.3: Quarkonia as a thermometer of QGP. Taken from [12] Left: An upper limit of the binding energy of different quarkonium states. Right: A cartoon representing therometer of QGP using quarkonia melting.

Thermal radiation

With the term thermal radiation are ment photons directly produced in the early stage of a collision. They leave the collision region without being affected by the medium. They might allow to study properties of QGP. Unfortunately, most of the measured photons are background, formed from hadron decays in the later stage of a collision, and it is necessary to distinguish those from the direct photons [4].

3.1 Parton energy loss and nuclear modification factor

High p_T partons, propagating through the dense medium, are supposed to loose energy. In particular, the energy loss is caused by two effects: by elastic collisions of partons in the medium and, more dominantly, by medium-induced gluon radiation (which is similar to bremsstrahlung of electrons). The energy loss is predicted to increase with the energy density of medium.

The significant energy loss of high p_T partons is treated as a probe of presence of QGP. As the QGP is supposed to be created in the central nucleus collisions, it is interesting to compare distributions of proton-proton (pp) and nucleus-nucleus (AA) collisions, as ilustrated in Figure 3.4.

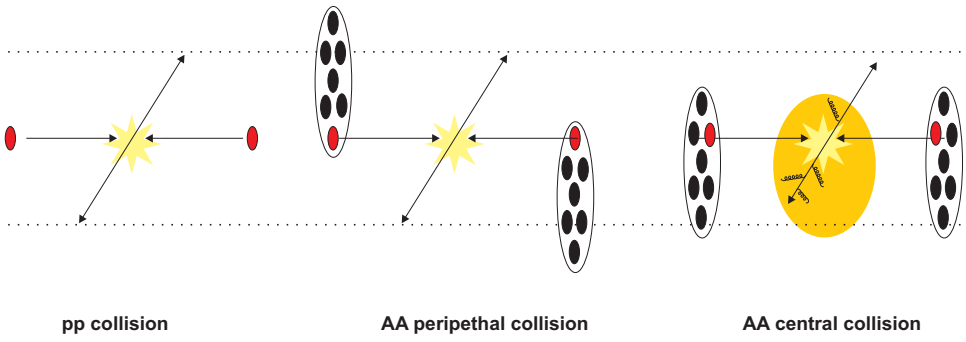

Figure 3.4: pp collisions, AA peripheral collisions and significant medium induced parton energy loss in the case of central AA collisions.

For this purpose nuclear modification factor $R_{AA}(p_T)$ is used [4]. With number of binary collisions N_{binary} known (i.e. from the Glauber model – see Appendix B), nuclear modification factor is defined as follows:

$$R_{AA}(p_T) = \frac{\frac{dN_{AA}}{dp_T}}{\langle N_{binary}(b)\rangle \frac{dN_{pp}}{dp_T}} \tag{3.2}$$

R_{AA} is a unity in case of no modification in high p_T particle production. If R_{AA} is smaller than one, the high p_T particle production is suppressed.

Alternatively, to compare distributions of peripheral and central AA collisions the central to peripheral ratio $R_{CP}(p_T)$ is used. $R_{CP}(p_T)$ is defined

as:

$$R_{CP}\left(p_T\right) = \frac{\langle N_{binary,centr}(b)\rangle \frac{dN_{per}}{dp_T}}{\langle N_{binary,per}(b)\rangle \frac{dN_{centr}}{dp_T}} \tag{3.3}$$

The results from nuclear modification factor measurement from STAR and ALICE experiments are shown in Figure 3.5 and Figure 3.6. It can be clearly seen, that the high p_T particles are suppressed in the nucleus-nucleus collisions compared to pp collisions. The reduction of high momentum particles in peripheral collision in contrast to central ones is also significant.

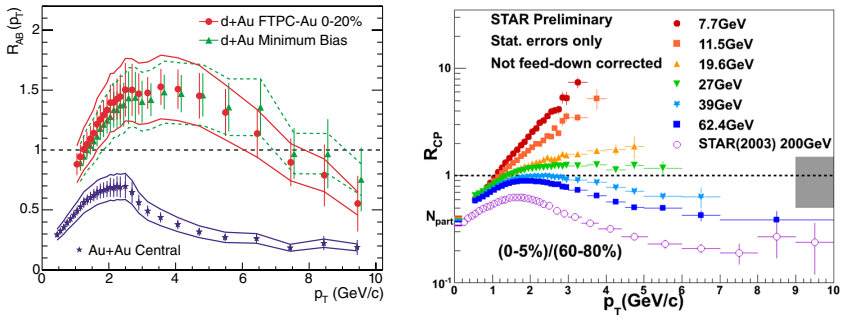

Figure 3.5: Left: R_{AA} measurement results from the STAR experiment, at $\sqrt{s_{NN}} = 200$ GeV AuAu central and peripheral and dAu collisions. Taken from [13]. Right: Measurements of R_{CP} for various energies (beam energy scan) from the STAR experiment. Taken from [14].

3.2 Jets and di-hadron correlations

Jets are collimated sprays of particles, flying out from the high energy collision region. All particles belonging to a single jet have originated from the same parton. This parton can be either quark, or gluon, created in the very early stage of the collision.

Due to the impulse-momentum conservation law, jets are created always in pairs, flying opposite each other in their center-of-mass reference frame. This can be observed in electron-positron or proton-proton collisions. In the case of central nucleus-nucleus collisions, when energy density in a collision region is very high and quark-gluon plasma can be created, the evolution of jet-pair is more complicated.

If the jet pair is created on the edge of the by collision created QGP medium, the jet closest to the edge leaves the collision region immediately without being affected by the medium. The other jet has to pass through the full hot medium and therefore is expected to be significantly modified. Studying jet modifications is predicted to provide important information about the properties of the medium. The jet measurements probe medium in its earliest stage. However, it is a challenging measurement, that suffers by high background.

Jet modifications can be studied indirectly via high p_T parton supression represented by nuclear modification factor, which is described in the previous

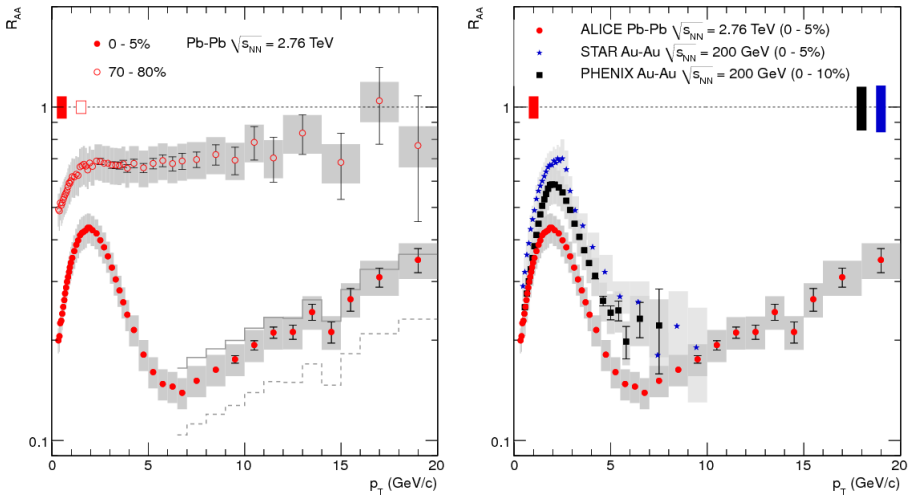

Figure 3.6: Left: R_{AA} measurement results from the ALICE experiment in central (0-5%) and peripheral (70-80%) PbPb collisions at $\sqrt{s_{NN}} = 2.76$ TeV, where R_{AA} represents comparison between central and peripheral collisions. Right: R_{AA} measurement results from the ALICE experiment ploted in comparison with STAR and PHENIX results at $\sqrt{s_{NN}} = 200$ GeV. Taken from [15].

section. The geometry of jet modification can be studied directly in di-hadron correlations, which is presented in the following text. The important jet characteristics are mentioned in the next chapter.

As shown in Figure 3.7, the di-hadron correlations are done by selecting high p_T particle, referred to as the *trigger*, and determining the distribution of the particles relative to that particle. The latter particles are referred to as the *associated particles*. In the $\Delta\phi - p_T$ space (see Appendix A), the peak related to the jet arising from the edge of a medium is plotted close to $\Delta\phi = 0$ and is referred to as *near side jet*. The peak close to $\Delta\phi = \pi$ is related to the jet opposite to the near side jet and is refered as *away side jet* [16].

The away side jet shows many interesting modifications between pp and AA collisions. The main effects to be studied in away side jet are azimuthal and pseudorapidity correlations.

3.2.1 Azimuthal correlations

As the away side jet penetrates through hot and dense medium, it looses energy. As depicted in Figure 3.7, the away side peak therefore would be suppressed (without shape modification and/or its shape would be modified.) Thie suppression is referred to as *jet quenching*. In AA collisions everything is complicated by the presence of collective flow, which causes the background modified by v_2 from E.q.(3.1), as shown in Figure 3.7.

The quenching was studied in pp and AA collisions. It has been shown, that compared to pp, where the near-side peak remains unchanged for all p_T, in the

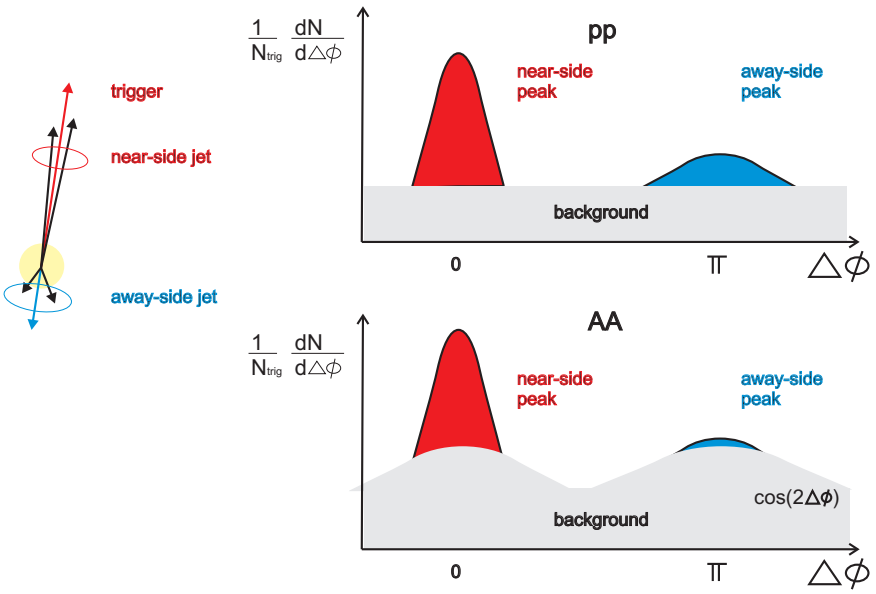

Figure 3.7: A schematic picture of two particle azimuthal correlation function, showing trigger particle, near side jet, away side jet and corresponding near side peak and away side peak. Up: Azimuthal correlations in pp collisions. Down: Azimuthal correlations in AA collisions, with background modified by v_2 from E.q.3.1.

case of AA collisions the away-side peak is only present for the highest partner p_T but is significantly suppresed for less energetic partners. The nature of energy loss, as well as energy distribution within quenched jet, the quenched jet structure and energy loss dependence of parton flavour will be studied in todays experiments, e.g. in STAR and ALICE. Di-hadron azimuthal correlations from the STAR experiment are shown in Figure 3.8.

Due to energy and momentum conservation laws, the missing intermediate p_T cannot dissapear. The missing p_T is supposed to be either shifted to lower energy (referred to as *softening*) and/or scattered into a broadened angular distribution (referred to as *broadening*). Both of these predictions have been observed [17].

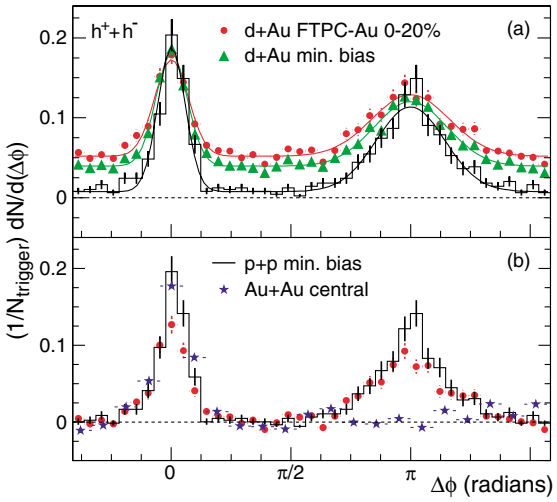

Figure 3.8: Di-hadron correlations in dAu pp and AuAu collisions at $\sqrt{s_{NN}}$=200 GeV from the STAR experiment. $N_{trigger}$ is the number of trigger particles within $4 < p_T, trigger < 6\text{GeV}/c$. The associated particles are taken from interval $2 < p_T, associated < p_T, trigger$ The supression of away side peak (*quenching*) in AuAu collisions is significant. Taken from [13].

3.2.2 Pseudorapidity correlations

Surprisingly, a modification of the near side peak is also observed, in the pseudorapidity (see Appendix A) region. It is formed by a wide associated yield out to $\Delta\eta = 4$, referred to as the *ridge*, which is shown in Figure 3.9. The ridge has been observed both in the STAR, PHOBOS, CMS, ATLAS and ALICE experiments in pPb, AA and also in very central pp collisions. It might be theoretically caused by parton energy loss in the medium (collisional, or radiative), collective motion of particles in the medium, or remnants from the initial state of a collision. Currently, the preferred scenario is, that the ridge is an image of fluctuations in the initial state [16].

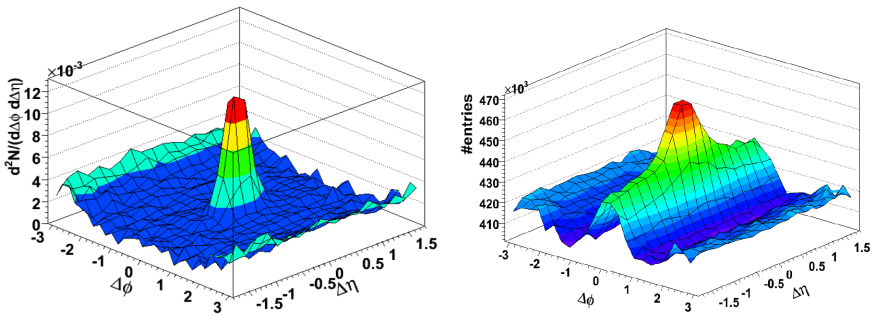

Figure 3.9: Di-hadron correlations from the STAR experiment in d+Au (Left) and 0-12 percent central Au+Au (Right) collisions at $\sqrt{s_{NN}} = 200$ GeV for 4.0 GeV/c $< p_{T,trigger} <$ 6.0 GeV/c and 2.0 $< p_{T,associated} < p_{triggerT}$. The angle $\Delta\phi$ is plotted in radians. In d + Au there is one peak on the near-side. This peak is shown also in the Au + Au but is surrounded by an additional correlation broad in $\Delta\eta$ that is referred to as the *Ridge*. Taken from [16].

Chapter 4

Jets as a probe of nuclear matter

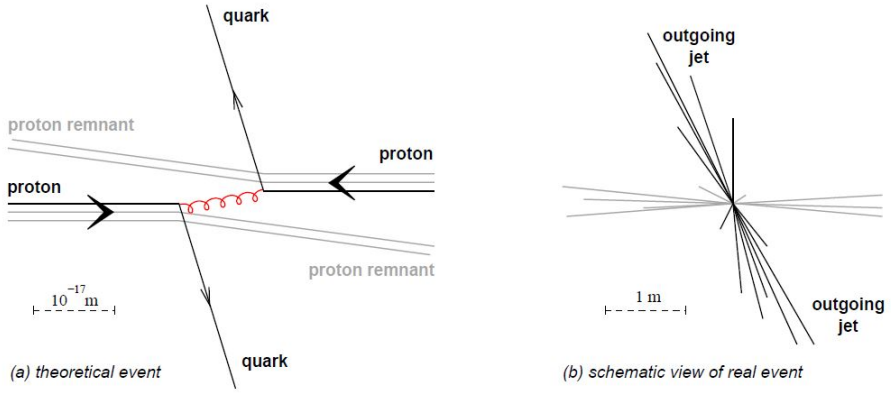

Figure 4.1: Jets as a connection of theoretical and real event and measured scales. Taken from [18].

4.1 Jet evolution

During its travel to detectors, jet undergoes a complicated process. A scattering of two partons (quarks or gluons) from each of the colliding nuclei results in the production of hadrons in the final state, that are measured in detectors. There are three levels of a jet [19], which are commonly distinguished and which are schematically depicted in Figure 4.2: parton level, particle level and calorimeter level.

Parton level

Parton level of a jet represents cluster of partons. This level is calculated in pQCD, allowing two types of processes- Leading Order (LO) and Next to Leading Order (NLO). Leading order processes are those, that are most probable, while next to leading order processes are lot less probable. An important next to leading order process is gluon radiation, which means, that quark can emit one or more gluons.

Particle level

At a particle level, jet is formed by hadrons in their final state. This level can be generated in Monte Carlo simulations.

Calorimeter level

Calorimeter level means energy towers, or other signals, collected by detectors in $\eta - \phi$ space. The way of interpreting the signal is referred to as *recombination scheme* and plays a crucial role in defining jets. The most common recombinational scheme is called *E-scheme* and will be discussed later.

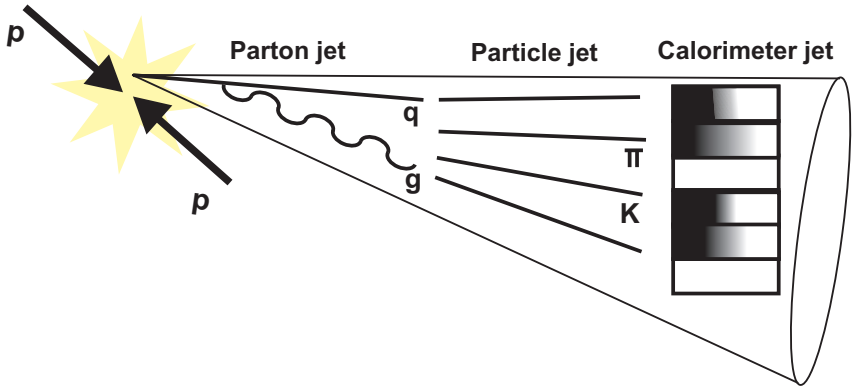

Figure 4.2: Various jet levels

4.2 Jet characteristics

In an ideal case, physicists would like to be able to measure by the partons from an initial state of a collision. Jets at the calorimeter level are the closest measurable observables to partons. This connection between jets and partons is illustrated in Figure 4.1. As the jet 3-momenta have the same direction as the original parton and as the sum of energy of a jet is the same as energy of original parton, the kinematics properties of the jet can correspond to the properties of original parton, so, in other words, by jet-reconstruction it is possible to "look back" into collision of partons.

The region of measured particles in azimuthal angle is often divided to three parts, according to the direction of jet with highest p_T (also called leading jet). The three regions are [20]: toward region, transverse region and away region.

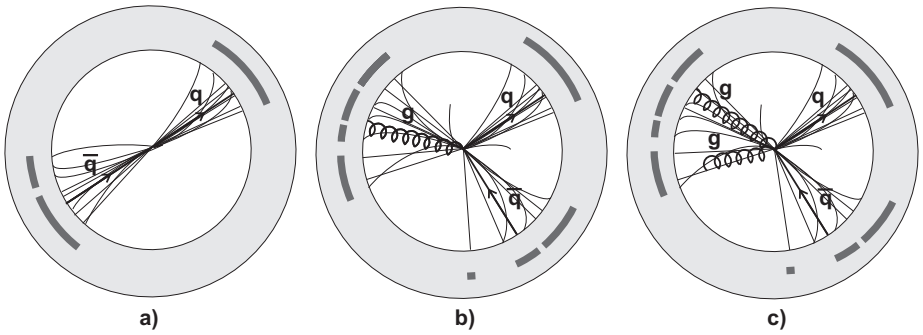

Figure 4.3: A schematic picture of a profile of a collider experiment with a dijet event (a) and trijet event (b), which can be classified as a 4jet event (c), according to jet finding criteria used.

Event, where two jets occur, is called a dijet event. As shown in Figure 4.3, there is a possibility, that one of the fragmenting quarks emits a high energetic gluon, that also fragments and makes a jet. Such an event is called a trijet event. Also events with more jets are possible, but with increasing number of jets in an event the propability decreases.

4.3 Jet background

When we want to link jets to the initial partons, the interested class of jets are jets from the *fireball* in the central part of a collision, where hard scattering occures. However, there are several scattering processes appearing in other parts of the collider tube. The field of study important as jets themselves is the jet background, appearing as a noise, that complicates the jet reconstruction. This background consists mainly of low p_T particles. There are three main sources [21] of jet background (as shown in Figure 4.4):

- Underlying event, which is formed by the collisions of remnants of all the scattering protons and multiparton interactions. It occures mainly in the transverse region.
- Pile-up, which is formed by additional p-p collisions from previous collisions of the beam.
- Background from the particles produced in the bulk in case of AA collision.

As there are many particles being created in a collision (especially in central collisions of heavy ions), it is not always intuitive to choose, which particle belongs to which jet. So, there is no exact definition of a jet. One event can be classified according to different criteria, and different number of jets can be found in the same event. To reconstruct jets, jet algorithms are used. They will be discussed in the next chapter.

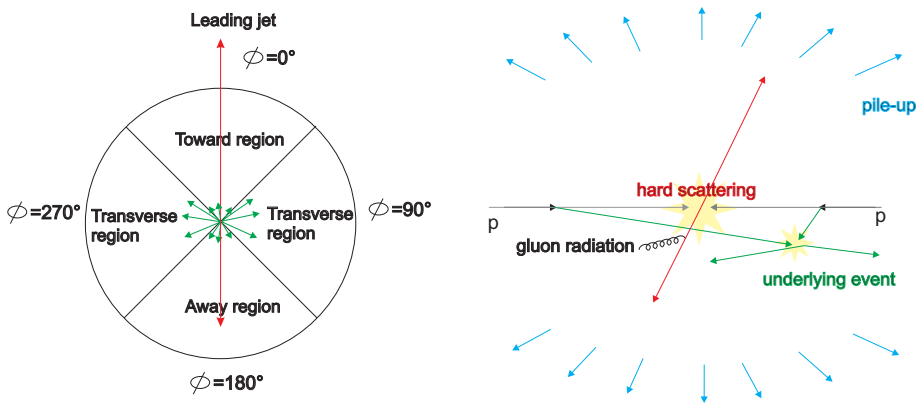

Figure 4.4: Left:A schematic picture of toward, transverse, and away jet regions classified according the direction of a jet with highest p_T. Right: Zoom into the collision region showing the mentioned sources of background.

Chapter 5

Jet algorithms

Jets are being reconstructed by selection processes – jet algorithms. These algorithms are supposed to link a set of measured signal from detector to an initial parton by reconnecting detected signal to jets, combining its momenta to form the momentum of a jet.

For simplicity, the signal from detectors (calorimeter towers, clusters, etc.) to be processed by a jet algorithm are traditionally referred to as *particles*. The procedure of connecting particles to jet is referred to as *clustering*.

Jets are being searched for in signals from a detector in η-ϕ space (see Appendix A). Computing the important observables of a jet, as four-momentum and transverse momentum, is made according to a specific recombination scheme. The commonly used recombination scheme is E-scheme, using observables defined as [19]:

$$p^J = (E^J, \vec{p}_J) = \sum (E^i, p_x^i, p_y^i, p_z^i), \tag{5.1}$$

$$p_T^J = \sqrt{(p_x^J)^2 + (p_y^J)^2}, \tag{5.2}$$

where E_i is energy and p_{ij} is momentum of particle i within a jet.

There are two main types of jet algorithms- seed and seedless. The seed algorithm starts by choosing starting particles (mostly the most energetic particles in the event) as seeds for an iterative process. The seedless algorithm starts without prechoice of seeds, it processes all calorimeter entries.

Commonly used jet algorithms can be divided to two following classes: cone and sequential-recombination, which basic principles are shown in Figure 5.1. Both are based on an assumption that all particles associated with the same jet are "nearby" each other [22]. Particularly, cone algorithms are finding jets by drawing narrow cones around the most energetic measured signals and defining everything within the cone to be part of the jet, whilst clustering algorithms are based on iterative connecting of particles until all of them are far apart enough.

5.1 Attributes of a reliable algorithm

It is important to notice, that jets do not have an exact definition independent of used algorithm. Every jet algorithm is just one possible view of a jet. It should be chosen according to our goals of study. But every reliable algorithm should

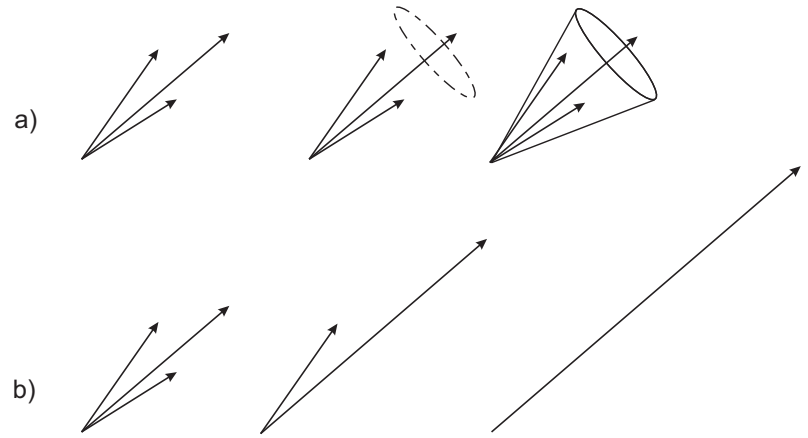

Figure 5.1: The basic principle of cone (a) and clustering (b) algorithms

fullfil following criteria: order independence, detector independence, collinear and infrared safety. All of them are discussed in paragraphs below [19].

Order independence

The same results at all jet levels- at parton level, particle level and calorimeter level should be obtained. This is very important, because we want to connect properties of the final state jet with those of initial parton.

Detector independence

The results of an algorithm should not depend of attributes (e.g. segmentation, energy response, size) of the detector, that provides the data.

Infrared and collinear safety

Adding a soft gluon (radiated by a parton as a NLO process) into an event shall not change final number of measured jets. This is called InfraRed (IR) safety. Splitting a given parton shall not change final number of measured jets. This is called collinear safety. Both the criteria are schematically shown in Figure 5.2.

Speed

As there are thousands of particles measured in detectors, especially in heavy-ion collisions, the algorithm should be as fast as possible. The time needed to find jet by the algorithm depends strongly on number of particles in an event. The speed of an algorithm is classified according to assymptotic computional complexity $O(g(N))$. Where N is the number of computed particles and $g(N)$ is a function. The typical multiplicity of an event for the Large Hadron Collider (LHC) and Relativistic Heavy Ion Collider (RHIC) experiments is in Table 5.1.

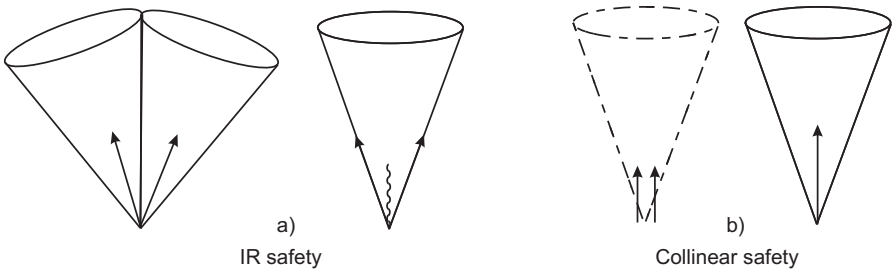

Figure 5.2: An example of a) Merging two jets to one jet, due to appearing infrared radiation in an event, referred as infrared unsafety. b) Treating two low energetic collinear particles as one particle with double momentum and adding them to a jet, referred as collinear unsafety.

Type of event	N
LHC ($\sqrt{s}$=14 TeV) dijet event	400
LHC low-luminosity event (5 pile-up collisions)	1000
RHIC Au-Au event ($\sqrt{s_{NN}}$=200 GeV)	3000
LHC high-luminosity event (20 pile-up collisions)	4000
LHC Pb-Pb event ($\sqrt{s_{NN}}$=5.5 TeV)	30 000

Table 5.1: Typical number of measured particles in LHC and RHIC. Taken from [23].

5.2 Cone algorithms

5.2.1 Seed cone algorithms

The seed cone algorithm chooses seeds for iterative process of looking for a stable cone, which is then called a jet. Seeds are defined as calorimeter entries above some minimum value of p_T [19]. Step by step, the cone algorithm defines for each seed a distance:

$$d_j = p_{Tj} \tag{5.3}$$

Then proceeds as displayed in the diagram in Figure 5.3.

Parameter R defines size of cone jet, and the jet has thus corresponding area $A = \pi R^2$. The value of R is defined by a user.

A key procedure of clustering cone jets is jet stabilization. In a stabilized cone jet, sum of the momenta of all particles in a jet has the same direction as the centre of the circle.

The splitting and merging procedure of overlapping cones is also important. If the fraction of shared energy is larger than 50 percent, jets are merged together. Otherwise, they are splitted.

There are two different ways of implementing cone algorithms, according to the way of dealing with jets that overlap. Both methods are defined in Figure 5.3.

- IC-SM (Iterative Cone with Split-Merge step)

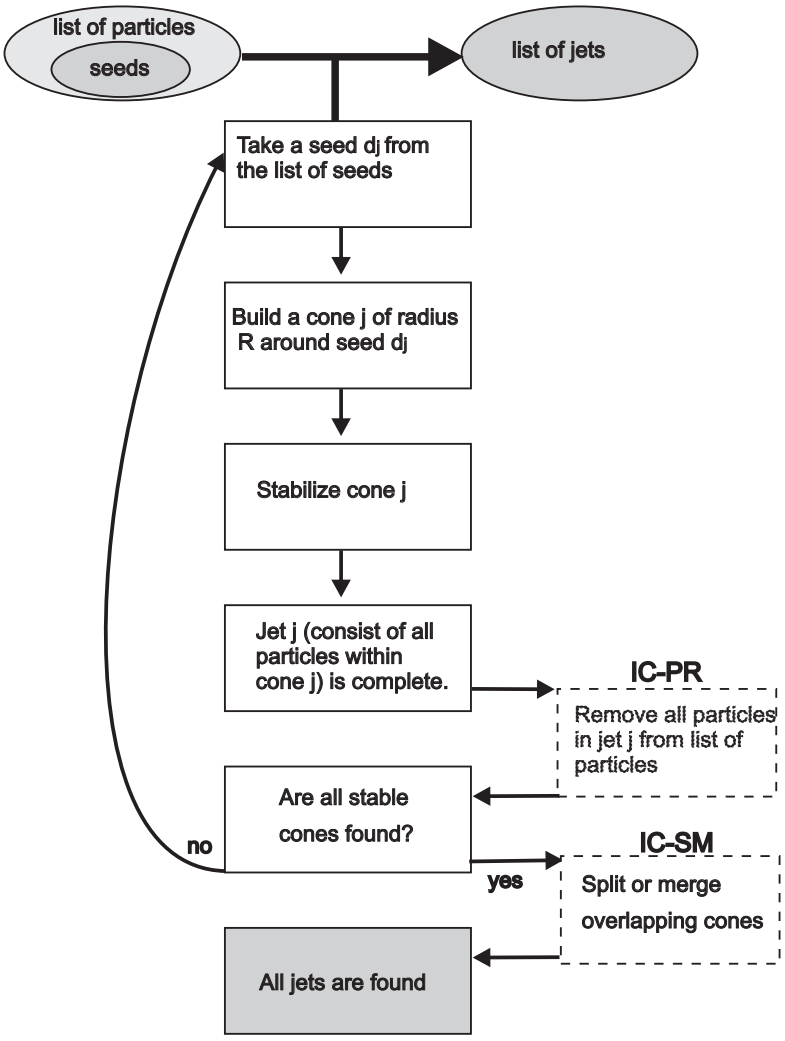

Figure 5.3: Schema of clustering by a seed cone algorithm.

- IC-PR (Iterative Cone with Progressive Removal of particles)

Output of the cone algorithm are stable cone jets. Because after the clustering process some particles are leaved outside the final volume of cones, not all particles are assigned to jets and some signal is lost. The cone algorithm benefits from its simple geometric construction that allows high speed of computing.

5.2.2 Seedless cone algorithms

An interesting seedless, IR and Collinear safe alternative to Cone algorithm is the SISCone (Seedless Infrared Safe Cone) algorithm [24]. Its principle in one dimension is depicted in Figure 5.4 and can be discribed as follows:

1. Put a circle of radius R into an event.
2. Move the circle in a random direction until it touches a point.
3. Rotate the circle around this point until it touches another one.
4. Particles in the circle form jet j.

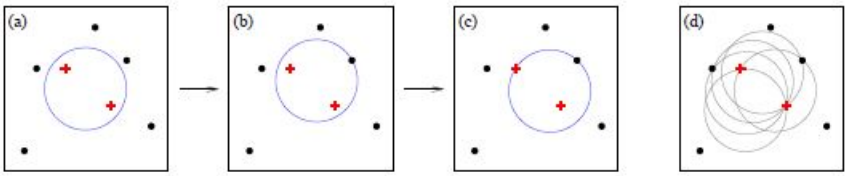

Figure 5.4: One dimensional demonstration of a SISCone algorithm. a) A circle is localized at a random position in $\eta - \phi$ space. b) The circle moves in a random direction until it touches a particle. c) Then, it starts rotating until it touches another particle. d) All possible final positions of a circle. Taken from [23].

5.3 Sequential-recombination algorithms

In contrast to cone algorithms, the sequential-recombination algorithms do not start with seeds, but they use all calorimeter tower entries, called preclusters [19].

Clustering algorithms start by defining two types of distances [25]:

- For each particle i define distance from the beam

$$d_j = p_{Tj}^{2k} \tag{5.4}$$

- For each pair of particles i, j define distance between i, j

$$d_{ij} = min(p_{Ti}^{2k}, p_{Tj}^{2k}) \frac{\Delta\eta^2 + \Delta\Phi^2}{R^2} \tag{5.5}$$

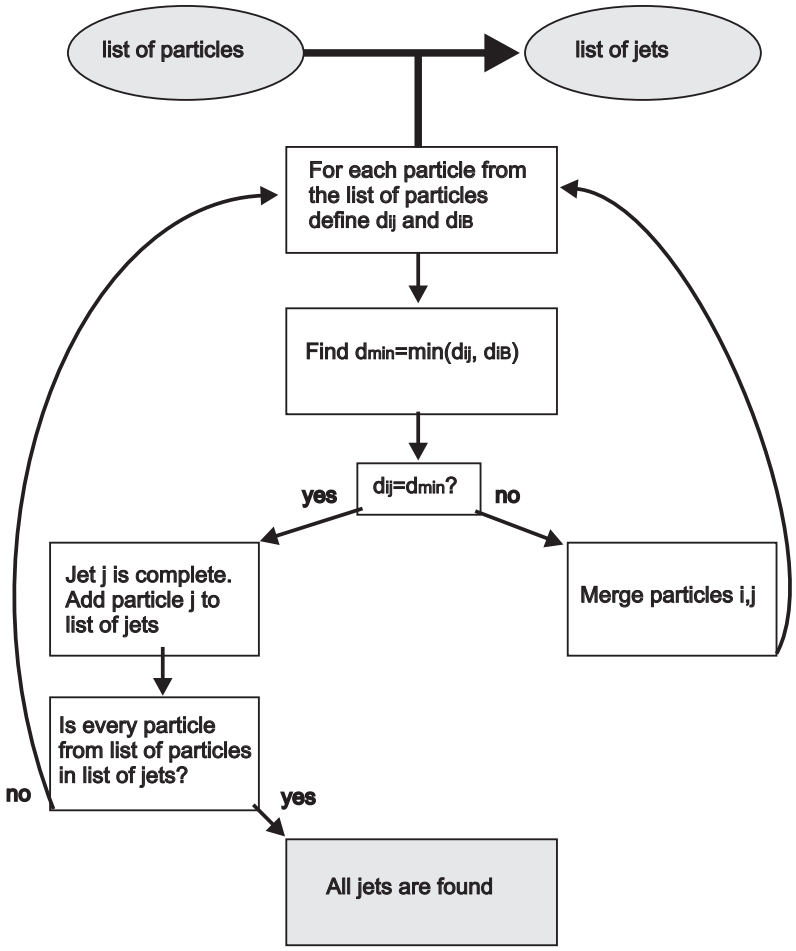

Figure 5.5: Schema of clustering by a sequential recombination algorithm.

Then, it clusters particles according to the scheme in Figure 5.5.
The merging of particles is defined as $\vec{p}_{ij} = \vec{p}_j + \vec{p}_i$, $E_{ij} = E_i + E_j$
There are two parameters to be specified before starting clustering algorithm:

- The parameter R controls termination of merging and modifies size of a jet.
- The parameter k represents the relative power of the transverse momentum p_T scale versus geometrical distance.

According to chosen value of parameter k, clustering algorithms are divided to [25]:

- k=1 k_T
  - This algorithm recombines closest particles with low p_T first. It is IR safe. However, due to prefering soft particles, itis sensitive to soft background, which is mainly of concern in AA collisions. As the clustering of this algorithm is easy to imagine, the step by step representation of it is displayed in Figure 5.6.
- k=-1 $anti - k_T$
  - This algorithm recombines highest p_T particles first. This implies, that soft particles are being recombined with hard ones before being connected among themselves, which leads to a perfect circularity of the hardest jets, as well as to IR and Collinear safety and order independence.
- k=0 $Cambridge - Aachen$
  - In this algorithm, clustering is based only on spatial separation, without taking particle momenta into concern.

The preference in clustering of particles, depending on momentum of a particle can be seen in Figure 5.7.

As there are no overlaping jets in the output of clustering algorithms, no split-merge steps are needed. Furthermore, every particle is assigned to an unique jet. All above mentioned clustering algorithms show a good order independence. The computing time of clustering algoritmhs grows as N^3, where N is the initial number of preclusters in an event. However, a faster version "Fastjet", with computing time growing as $NlnN$ for large N, has been developed. Detailed study of Fastjet can be found in [26]. The comparison of speed of all algorithms can be seen in Figure 5.8.

The overview of all mentioned algorithms, including their IRC safety and speed can be seen in Table 5.2. The comparison of output (size, circularity) of the mentioned algorithms is presented in Figure 5.9.

5.4 Jet areas

As a jet consists of pointlike particles, which themselves have no area, it is necessary to find a method to define area of a jet [27]. Particularly this is done

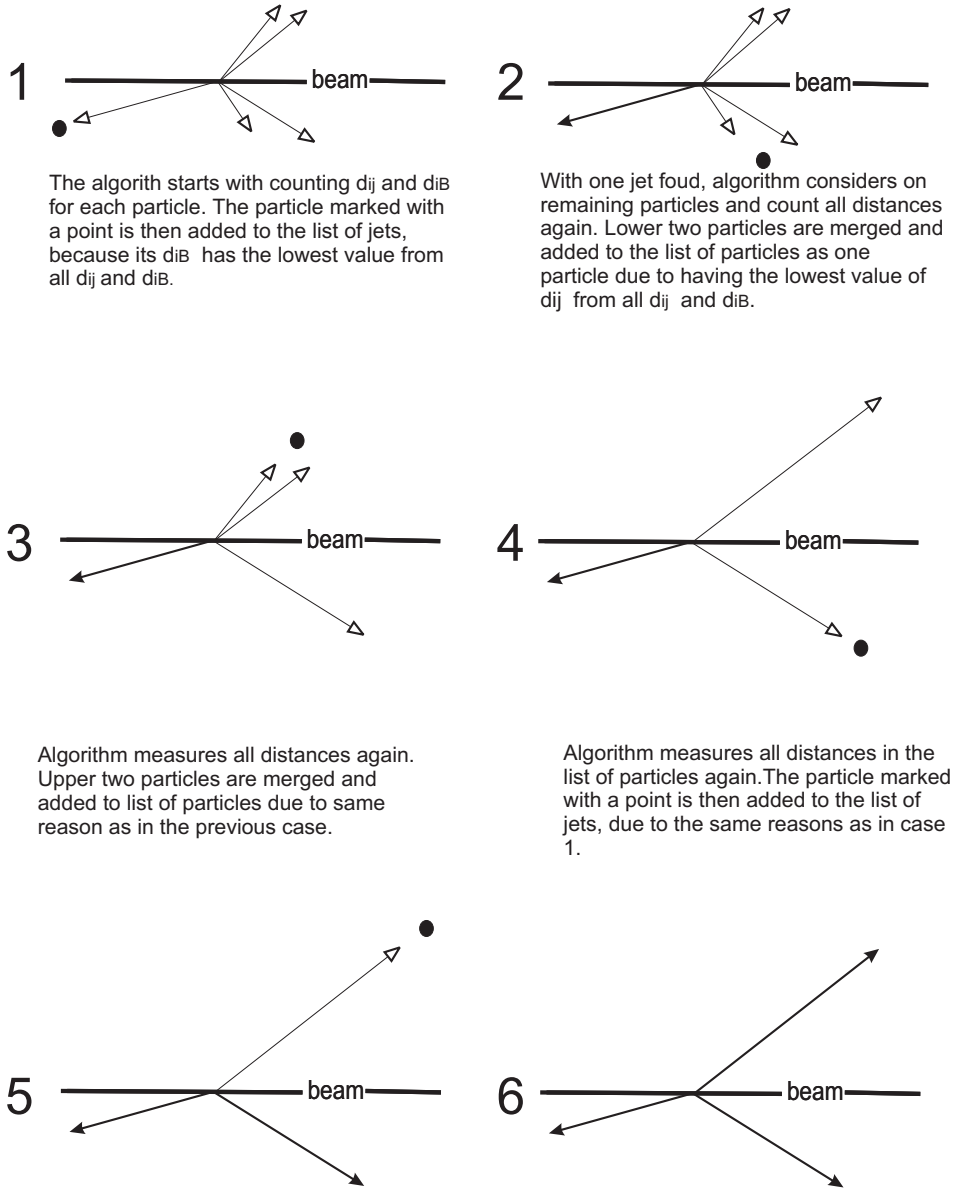

Figure 5.6: The step-by-step schematic picture of clustering particles to jet by a k_T algorithm.

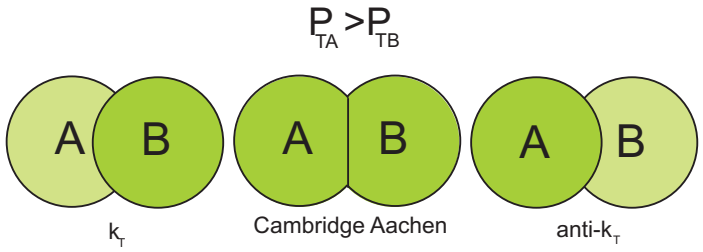

Figure 5.7: Preferences in clustering according to particle momentum by k_T, anti-k_T and *Cambridge-Aachen* algorithms.

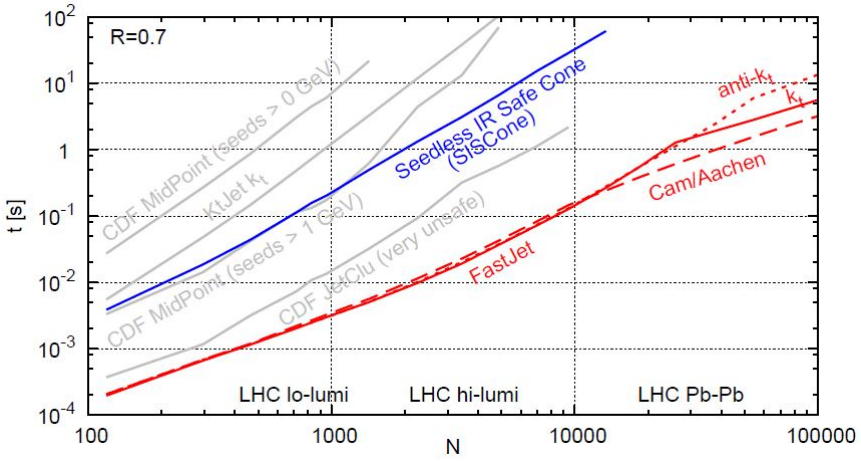

Figure 5.8: A comparison of computing time of various algorithms according to the number of particles in an event, N. Taken from [23].

	IR safety	Collinear safety	Speed
Cone	no	no	N
SISCone	yes	yes	$N^{3/2}$
k_T	yes	yes	$N \ln N$
$anti - k_T$	yes	yes	$N \ln N$
$Cambridge - Aachen$	yes	yes	$N \ln N$

Table 5.2: Comparison of all described jet algorithms [23].

by adding very soft (low p_T) particles (which are referred to as *ghosts*) into an event and clustering them with a jet. The region in which a jet is able to catch a ghost is then called area. This definition is meaningful only for an IR safe algorithm, where addition of a ghost will not alter the clustering of hard particles. By definition, jet areas show us the susceptibility of an algorithm to catch soft background, and therefore can be used to subtract it.

Passive area

One soft ghost is added into an event. The passive area corresponds to pointlike radiation and with one hard jet in an event acts as πR^2[27].

Active area

Many uniformly distributed soft ghosts are added into an event. In contrast to passive area, while clustering an active area, soft ghosts can also cluster among themselves. This results to a possibility of ending up with jets made only of ghosts. In contrast to circle-like passive area, the active area has a complicated structure (see Figure 5.9). It corresponds to a diffuse radiation [27].

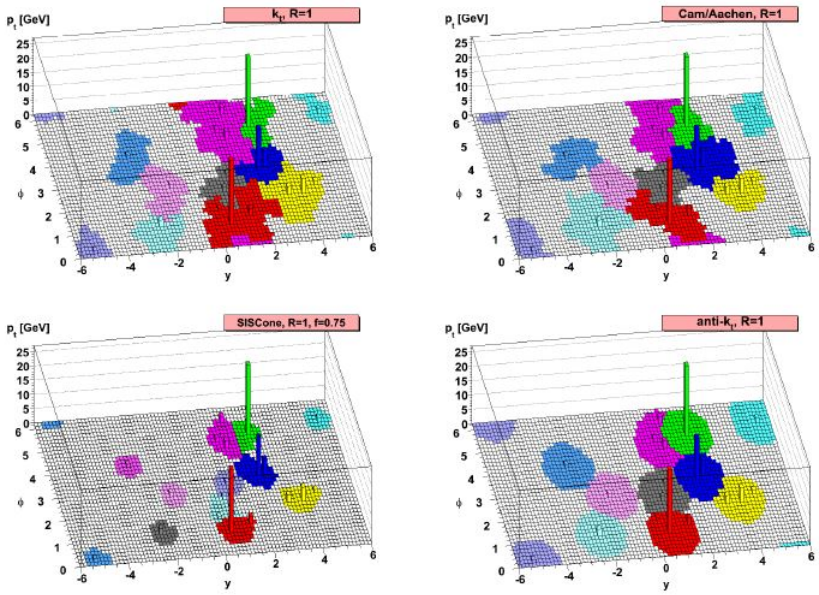

Figure 5.9: Comparision of final jets and their areas after clustering an event at parton level by four different algorithms. Taken from [25]

5.5 Decontamination of a jet

An important field in jet analysis is background subtraction, referred to as decontamination of a jet. In the ALICE experiment, this is done by using jet

areas. This method will be discussed in the section below. The main sources of soft background are discussed in the previous chapter.

5.5.1 Decontamination using background density

To subtract contamination of a jet, one can use jet areas. This type of subtraction is made after the jet finding has been carried out. The background density of transverse momenta ρ is defined as follows [28]:

$$\rho = median\{\frac{p_{T,i}}{A_i}\}, \tag{5.6}$$

where $p_{T,i}$ is the transverse momentum of a jet i and A_i is the area of a jet i.

The momentum of each jet is then corrected on average as [28]:

$$p_{T,jet,true} = p_{T,jet,reconstructed} - \rho A \tag{5.7}$$

Or, if needed, in a vector form:[28]

$$p^{\mu}_{T,jet,true} = p^{\mu}_{T,jet,reconstructed} - \rho A^{\mu} \tag{5.8}$$

Due to its properties, for defining background density is used k_T algorithm, while for jet reconstruction the $anti - k_T$ algorithm [28].Dependence of charged particle background density ρ on uncorrected multiplicity of tracks used for jet finding is shown in Figure 5.10.

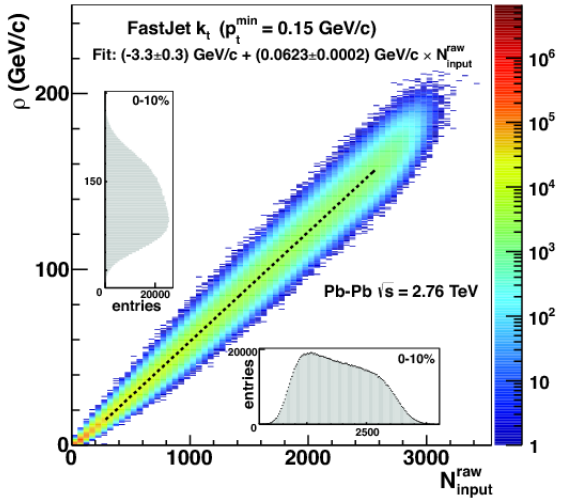

Figure 5.10: Dependence of charged particle background density ρ on uncorrected multiplicity of tracks used for jet finding. The insets show the projected distributions of ρ and raw multiplicity for the 10% most central events PbPb $\sqrt{s_{NN}} = 2.76$TeV measured by ALICE. Taken from [29].

5.6 Jet substructure

The jet constists primarily of hadrons in final state. At high p_T, most of them are protons and pions. Final state particles are directly identified via PID (Particle IDentification) detectors. The PID capabilities of the ALICE experiment will be discussed in the next chapter.

The shorter living particles, that decay before reaching the detector, can be identified by their theoretically known decay. The measured particle is assigned to a *primary vertex* and the decay products arise from the *secondary vertex*, as is depicted in Figure 5.11.

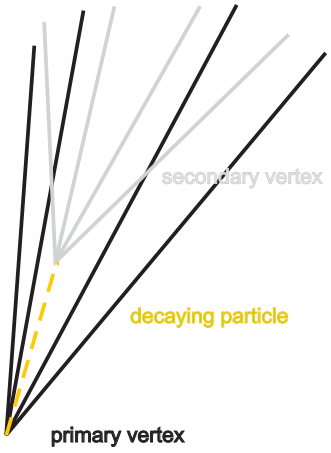

Figure 5.11: Primary and secondary vertex within a jet.

5.7 Jet shapes

The first more detailed insight into a jet, to find out some information about the internal angular distribution of hadrons within it, can be done by describing the distribution of energy within a jet, using the transverse momentum density at some circle of the radius $r < R$,$r = \sqrt{\Delta\eta^2 + \Delta\phi^2}$, with centre in the axis of the jet. This tool to observe jet substructure is called jet shapes [30] (sometimes also jet profile). There are two types of jet shape- differential and integral. Both are shown in Figure 5.12.

Differential jet shape $\rho(r)$ is defined as an average fraction of total p_T of a jet inside an annulus of radius Δr concentric to the jet cone axis.

$$\rho(r) = \frac{1}{N_{jets}} \lim_{\Delta r \to 0} \sum_{jets} \frac{p_T(0, r + \Delta r) - p_T(0, r)}{p_T(0, R)\Delta r} \tag{5.9}$$

Integrated jet shape is defined as fraction of total p_T of a jet of radius R inside a sub-jet of radius $r < R$, which is concentric to the jet cone axis.

$$\psi(r) = \frac{1}{N_{jets}} \sum_{jets} \frac{p_T(0, r)}{p_T(0, R)} \tag{5.10}$$

Where N_{jets} is number of jets, which are taken into account, and $pT(0, r)$ is sum of p_T of all particles within the concentric subjet. By definition $\psi(0) = 0$. It is normalized as $\psi(R) = 1$, i.e. the fractional transverse momentum of the signals inside a subjet of radius equal to the jet cone radius around the jet axis is unity. By definition, $\psi(r) = \int_0^r \rho(r)dr$.

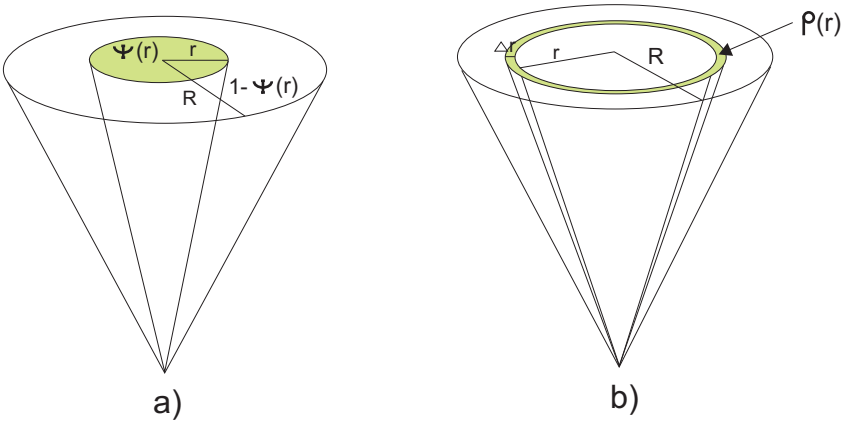

Figure 5.12: Jet shapes. a) integral jet shape b) differential jet shape.

Important characteristic of jet shapes is, that they are sensitive, whether the parton from the initial stage of a collision, from which was the jet formed, was quark, or gluon. Furthermore, if the jet is formed by a quark, they are sensitive to its flavour.

Chapter 6

High energy collision experiments

In the past 25 years, the search for QGP experienced a significant development. A brief summary of important experiments, with further insight to the ALICE detector at Large Hadron Collider (LHC) at CERN, will be discussed in this chapter.

6.1 Important experiments

SPS

The first evidence of existence of QGP was at Super Proton Synchrotron (SPS) at CERN in 1990s. The SPS is an accelerator, that provided experiments with a fixed target. Different aspects of PbPb and PbAu collisions were measured by seven experiments: NA44, NA45/CERES, NA49, NA50, NA52/NEWMASS, WA97/NA57, and WA98. The first experiments used relatively light nuclei such as oxygen and sulphur. A second generation of experiments using lead ions started data taking from 1994. After the whole analysis was finished in 2000,the combined results gave compelling evidence that QGP had been created [31]. Currently, the SPS provides beams for LHC.

RHIC

In 2000, the Relativistic Heavy Ion Collider (RHIC) was built at Brookhaven national laboratory in the USA. At RHIC, hot and dense nuclear matter and QGP in large variety of collisions at broad range of energies is studied. The pp collisions were studied at $\sqrt{s} = 62$ GeV, $\sqrt{s} = 200$ GeV and $\sqrt{s} = 500$ GeV. The AuAu collisions were studied from $\sqrt{s_{NN}} = 7$ GeV up to $\sqrt{s_{NN}} = 200$ GeV. The dAu collisions were studied at $\sqrt{s_{NN}} = 200$ GeV. The CuCu collisions were studied at $\sqrt{s_{NN}} = 62.4$ GeV and $\sqrt{s_{NN}} = 200$ GeV. The UU collisions were studied at $\sqrt{s_{NN}} = 193$ GeV [32]. The RHIC program started with four experiments- BRAHMS, PHOBOS, PHENIX and STAR. In present days, two of them, PHENIX and STAR, are active. RHIC observed existence of QGP phase transition. Its equation of state, however, remains unknown [33].

	SPS	RHIC	LHC
Initial temperature [GeV]	0.38	0.6	> 1
Initial energy density [GeV/fm^3]	~ 5	~ 25	~ 250
Freeze-out volume [fm^3]	$\sim 10^3$	$\sim 10^4$	$\sim 10^5$
Life time [fm]	< 2	$2 - 4$	> 10

Table 6.1: Medium characteristics in the SPS, RHIC and LHC experiment. Taken from [22].

LHC

At LHC, the experiments reach energies about 300 times higher than at SPS and 30 times higher than at RHIC [22]. This might allow creation of hotter, larger and longer living QGP, that would be easier to study. The energies are supposed be high enough to produce hard probes copiously and enable full reconstruction of hadronic jets [34].

LHC ist located at CERN in Switzerland on the border with France. CERN (European Organization for Nuclear Research) is the world's largest particle laboratory, which provides infrastructure needed for high-energy physics research.

There are four main experiments at LHC: ALICE, ATLAS, CMS and LHCb. Data were collected at $\sqrt{s} = 0.9$ TeV, $\sqrt{s} = 2.76$ TeV, $\sqrt{s} = 7$ TeV in pp collisions, at $\sqrt{s_{NN}} = 5.02$ TeV in pPb collisions and at $\sqrt{s_{NN}} = 2.76$ TeV in PbPb collisions [35].

The medium characteristics in the SPS, RHIC and LHC experiment are in Table 6.1.

6.2 ALICE

The ALICE experiment [35] [36], which is depicted in Figure 6.1, is designed to study strong interacting matter and quark-gluon plasma. It has total volume of 16×16×26 m^3, weight 10 000 t and consists of 18 detector subsystems. It is supposed to identify particles and their tracks from very low (100 MeV/c) up to high (100 GeV/c) transverse momenta. Furthermore, ALICE is able to deal with high particle density (up to 8000 particles per unit rapidity, resulting in up to 20 000 tracks from secondary vertices) [35], which allows more detailed analysis of jet structure, e.g. The main tracking detectors cover full azimuthal angle, which is important for azimuthal correlations of quenched jets [7] [22].

The subdetectors can be divided to three major subsystems:

- Central barel detectors, which cover polar angles from 45° to 135° and full azimuth. They are located in the midrapidity region ($-0.9 < \eta < 0.9$) within L3 magnet (12m long, radius 5m) providing magnetic field 0.5 T[36].
- Forward muon spectrometer, which is located in the region $2.5 < \eta < 4.0$.
- Forward detectors in the pseudorapidity region $\eta > 4$.

A detailed summary of all detectors and performance can be found in [35] and [36]. In this thesis, only those detectors most important for jet analysis will be briefly discussed.

Measured jets are divided to charged jets (consists only of charged particles) and full jets (consist of charged and neutral particles). Charged jets are formed from charged tracks measured in the Time Projection Chamber (TPC) and the Inner Tracking System (ITS). Full jets are formed both from tracks and clusters within the Electromagnetic Calorimeter (EMCal).

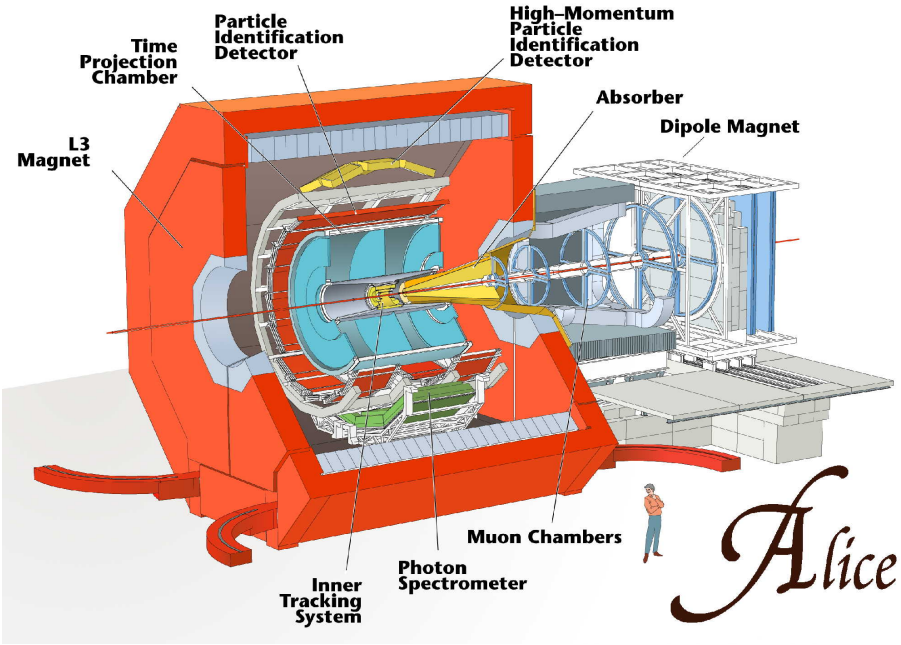

Figure 6.1: The ALICE experiment. Taken from [37].

All of them will be briefly discussed in sections below.

6.2.1 Inner Tracking System

ITS (see Figure 6.2) is the closest detector to the beam pipe. It consists of three concentric layers, each containing two silicon detectors, located at radii r = 4, 7, 15, 24, 39 and 44 cm. The innermost layer consists of two silicon pixel detectors (SPD). The middle layer consists of two silicon drift detectors (SDD). The outermost layer consists of two silicon strip detectors (SSD). It covers rapidity range of $\eta = 0.9$.

ITS is used for tracking and finding position of primary vertex and secondary vertices of heavy flavour weak decays. It can also improve momentum and angular resolution of high p_T particles. Furthermore, it reconstructs tracks of low p_T particles, which do not reach the TPC. Except the innermost two layers of detectors, it can provide particle identification by measuring energy loss per unit path length $\frac{dE}{dx}$ (see Appendix C) [38].

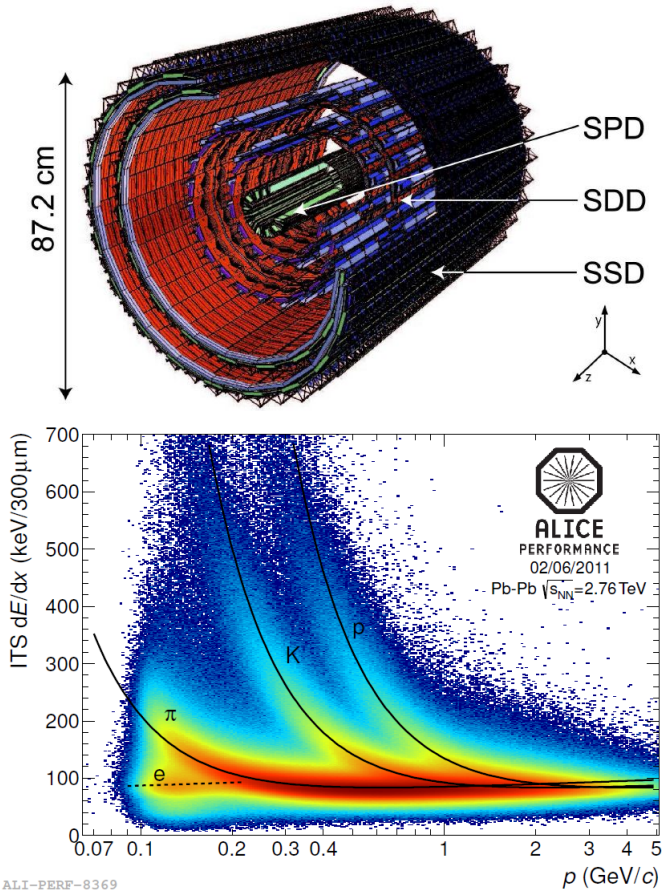

Figure 6.2: Up: Layout of ITS detector. Down: Particle identification from ITS. Taken from [39].

6.2.2 Time Projection Chamber

TPC (see Figure 6.3) is the main tracking detector for charged particles in ALICE. It is positioned at 85 cm from the beam pipe. Its length along the beam direction is 500 cm. It has a large volume of nearly 87 m^3, which makes it the largest time projection chamber in the world. It is filled with a gas of mixture of Ne and CO and N2 (85.7/9.5/4.8%) [40]. In the middle of the cylindric chamber, the high voltage thin electrode is located. It provides uniform electric field. The parallel magnetic field is also applied. On both ends of the cylinder, the readout planes are positioned. They contain cathode pads and anode wires. Each of the two readout planes is composed of 18 inner and 18 outer chambers with a total of 159 pad rows, resulting in a total of 557 568 pads.

As the charged particle penetrates through the gas, it ionizes it. The by ionisation produced electrons are driven by the electric field to the read-out chambers and anode wires. From here, they come to the pads, where the charge is interpreted as position of particle in x-y plane. The z coordinate is given by the difference between the trigger time and the arrival time of the signal to the pads. The own particle identification is made according to the amplitude of the signal, which is relative to the energy loss of a particle [38] . TPC measures ionization energy loss $\frac{dE}{dx}$ (see Appendix C).

TPC is used for full primary and secondary vertex reconstruction, track separation momentum measurement and particle identification. Along a track, a maximum of 159 clusters can be measured.

6.2.3 Time Of Flight detector

The TOF detector (see Figure 6.4) is placed at 3.7 m from the beam pipe and covers cylindrical surface of 160 m^2. It identifies particles by measuring the time difference Δt between the time when particle reaches T0 detector (see [36]) and TOF detector. With the calculated value of velocity together with particle momentum obtained from TPC, the particle mass can be calculated. TOF provides measurement of medium p_T particles, such as 2.5 GeV/c for pions and kaons and 4 GeV/c for protons.

TOF consists of 1638 strips of Multi gap resistive plate chambers, positioned in gas tigh modules transversely to the beam direction, covering an area of 160 m^2 with 157248 readout channels (pads). The high electric field is uniform over the full sensitive gaseous volume. A ionisation of a through-going particle immediately starts an avalanche, which generates observed signal on the pick up electrodes [41]. Its time resolution is about 80 ps [38].

6.2.4 Electro-Magnetic Calorimeter

The EMCal (see Figure 6.5) is a late addition to ALICE. It is positioned 4.5 m from the beam pipe and covers azimuthal angle 107° and pseudorapidity range $\eta < 0.7$. It is a Pb scintilating calorimeter, which comprises almost 13.000 individual towers that are grouped into ten super-modules. Incoming particle initiates a particle shower, containing electron-positron pairs and photons. Composition of this shower and its dimension depends on the particle type and detector material. The EMCal measures neutral component of jets, mainly photons and provides fast online trigger [43].

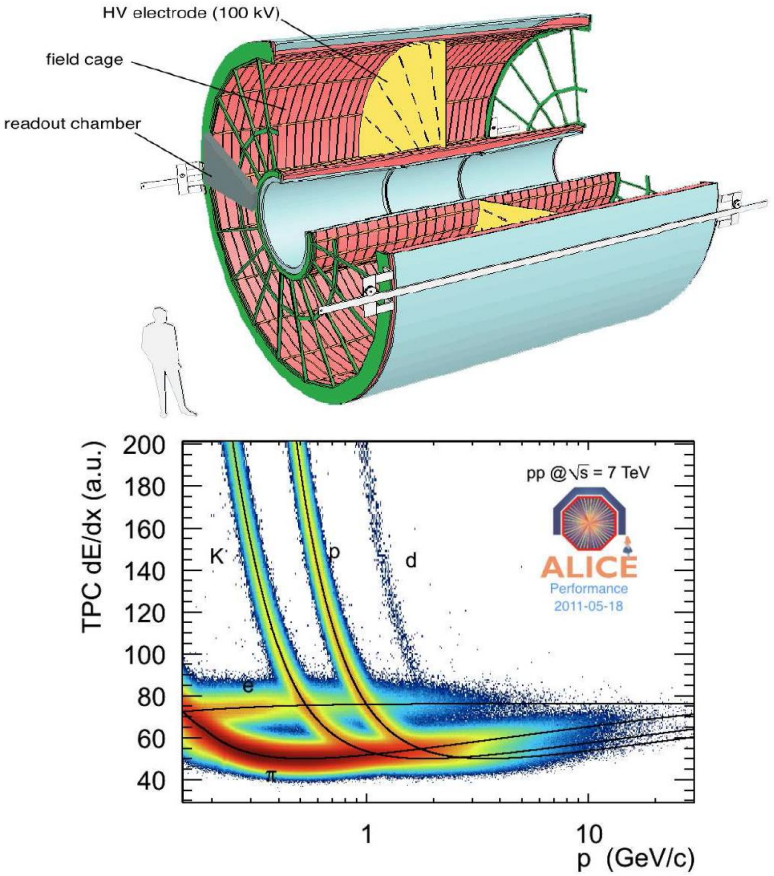

Figure 6.3: Up: Layout of TPC detector. Down: Particle identification in TPC. Taken from [38].

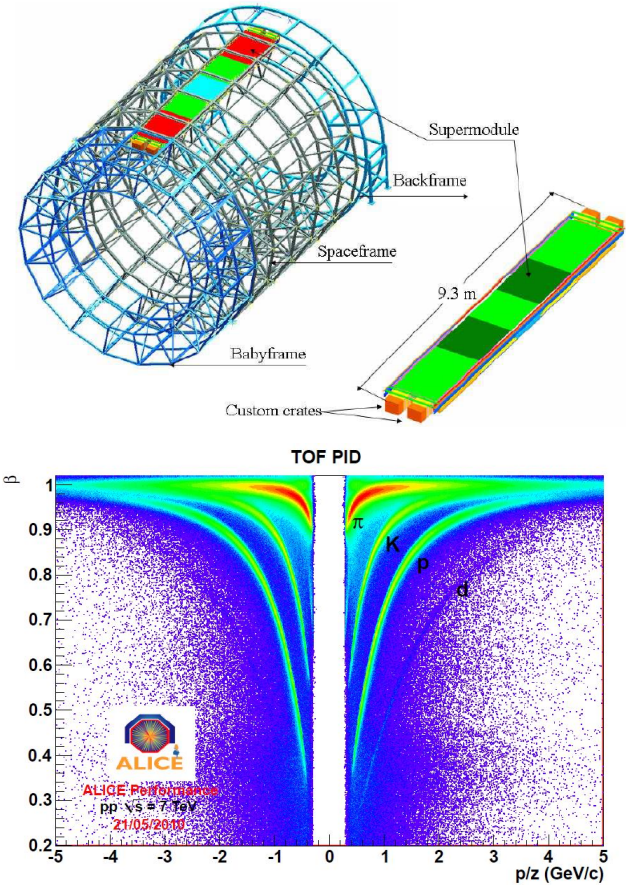

Figure 6.4: Up: TOF detector. Taken from [42]. Down: Identification of particles at TOF. Taken from [38].

At present the Di-jet Calorimeter (DCal) is being developed. DCal has the same structure as EMCal. They both will be placed back-to-back in azimuth.

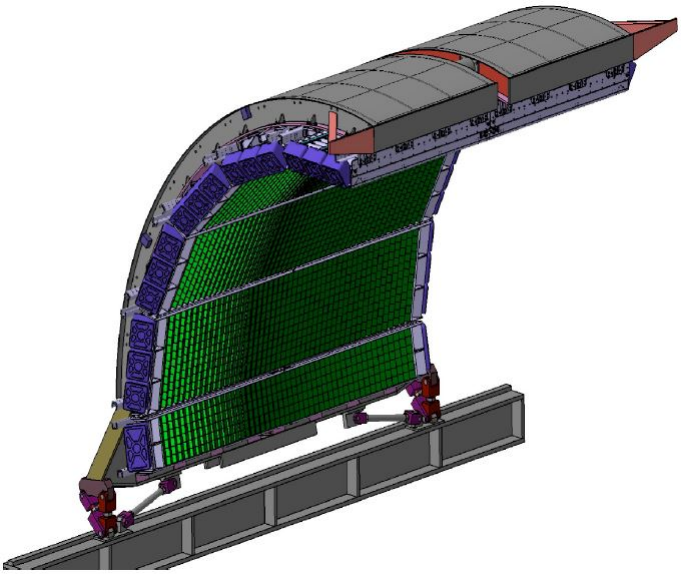

Figure 6.5: Layout of EMCal detector. Taken from [43].

Chapter 7

Topological reconstruction of strange particles

Short living particles are identified via their decay products, which are referred to as *daughters*. The method of their identification is referred to as *topological reconstruction*. Its principle will be shown on an example of identification of strange particles in jets, for which is this method crucial.

The strange particles can be grouped into three main classes according to their decay topology [39]:

- V0 topology: $K^0_s \to \pi^+\pi^-, \Lambda \to \pi^- p$;
- Cascade topology $\Sigma^- \to \pi^-\Lambda \to \pi^-\pi^- p$ and $\Omega^- \to K^-\Lambda \to K^-\pi^- p$;
- Kink topology $K^\pm \to \mu^\pm\nu(\bar{\nu})$;

The first step of topological reconstruction is choosing a decay channel and its corresponding topology, that is probable enough and contains preferentially charged particles (in order to be easily measured by detectors). All charged tracks are then reconstructed and extrapolated to primary vertex.

7.1 Cuts

There are several quality selection criteria [40], referred to as *cuts* that can be applied to the data, in order to improve the quality of results. The commonly used cuts are event cuts, track cuts and secondary vertex cuts.

Event cuts

The procedure is started by the event selection. The typical cuts, that can be applied are:

- Centrality
- Pileup filters – in order to set the most appropriate pile-up subtraction methods.
- p_T of the hardest jets – the events with low p_T jets are removed in order to avoid detection inefficiencies.

Track cuts

The cuts are also applied at all the tracks of the selected event. One can apply a cut to:

- Pseudorapidity of a track – in order to match the detector coverage.
- Required detectors – in order to detect all decay products.
- Position in a detector – in order to reject primary vertices too far from the center of the detector.
- Number of clusters within the track – in order to avoid bad reconstructed trajectories.
- N(σ) – in order to reduce background at low p_T. N(σ) is width of the energy loss distribution from the PID detector (see Chapter 6), where σ is obtained from a Gaussian fit. Examples of such distribution width ($\pm 5\sigma$ and $\pm 3\sigma$) are schematically depicted in Figure 7.1.

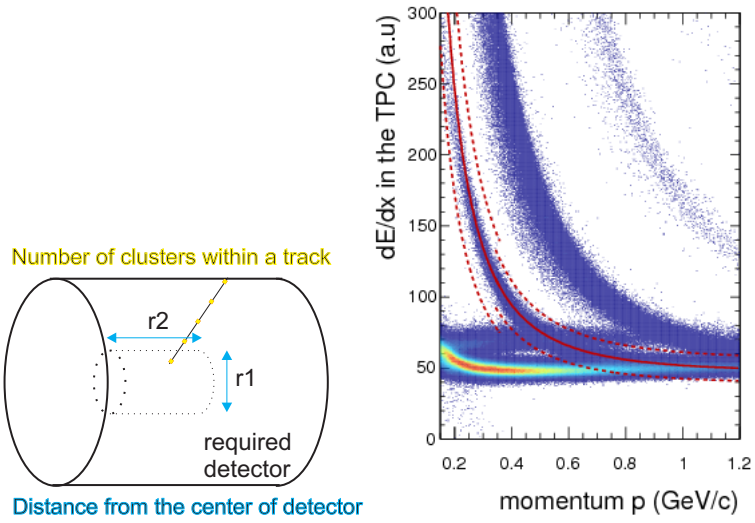

Figure 7.1: Typical cuts used in reconstruction of tracks. Left: Number of clusters within the track and position within the detector. Right: The distribution of the measured energy-deposit of charged particles versus their momentum in the TPC. The dashed lines delimit successively a $\pm 5\sigma$ then a $\pm 3\sigma$ selection of the kaon tracks. Taken from [40].

Secondary vertex cuts

To find the position of secondary vertex, cuts are also applied to some typical topological distances, namely:

- Minimum and maximum decay length – in order to improve the quality of the V0 selection. Decay length is equal to $c\tau$, where τ is the lifetime of the particle.

- The distance of closest approach (DCA) of a daughter track to primary vertex and DCA between daughter tracks – in order to improve the quality of the V0 selection.
- Cosine of pointing angle – in order to have as much particles as possible deriving from the primary vertex, it must be close to 1.

The above mentioned common cuts can be seen in Figure 7.1 and Figure 7.2.

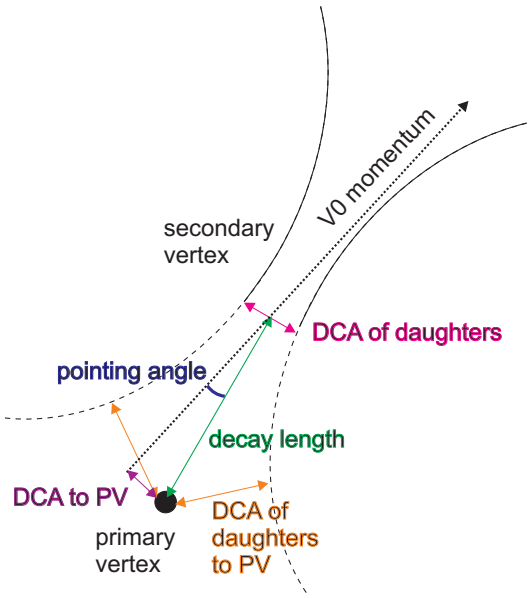

Figure 7.2: Schematic picture of topology of V0 decay and commonly used cuts in topological reconstruction of secondary vertex.

7.2 Invariant mass

Mass for each candidate is calculated using measured momentum of daughter tracks and known mass of daughters. The invariant mass histogram is used to determine the number of produced particles, referred to as *yield*.

7.3 K^0_s and Λ uncorrected yield analysis

I have analyzed the uncorrected Λ and K^0_s yield for 5 intervals of V0 transverse momentum (0-1 GeV/c, 1-2 GeV/c, 2-3 GeV/c, 3-6 GeV/c, 6-9 GeV/c).

I used data collected from the ALICE experiment from Run10 PbPb collisions $\sqrt{s_{NN}}$ =2.76 TeV, 0-80% centrality. The data were prepared by a Ph.D. student at NPI, Vít Kučera.

The data included events with hard jets found by anti-k_T algorithm (R=0.4, $p_T > 150$ MeV/c). The background was estimated using E.q.(5.7). The background density was found by k_T algorithm (see Chapter 5). The data contained

centrality	0-80 %
hardest jet p_T	>5 GeV/c
jet $\|\eta\|$	< 0.35
required detector	TPC
crossed TPC pad rows	≤ 70
$\|\eta\|$ of a track	≤ 0.8
radial fiducial boundaries	0.9-100 cm
N(σ)	$\leq 3\sigma_{dE/dx}$
DCA of daughters to primary vertex	≥ 0.1 cm
DCA between daughters	$\leq 1\sigma_{TPC}$
cosine of the pointing angle	≥ 0.998
$\|\eta\|$, $\|y\|$ of V0	≤ 0.75
proper lifetime	$\leq 3\tau$

Table 7.1: Cuts applied on events, tracks and secondary vertices

Particle	Quark content	Mass (MeV/c^2)	Decay length $c\tau$ (cm)
Λ	uds	1115.683 ± 0.006	7.893 ± 0.060
K_s^0	$\frac{d\bar{s}-s\bar{d}}{\sqrt{2}}$	497.648 ± 0.022	2.6859 ± 0.0015

Table 7.2: Characteristics of K_s^0 and Λ. Taken from [44].

also raw information on Λ and K_s^0 signals found in events via the V0 topology. Important used cuts are summarized in Table 7.1. The important characteristics of Λ and K_s^0 are in Table 7.2.

My work was to estimate background and calculate the yields (number of particles inside the signal, where signal means the invariant mass peak) for various p_T intervals. To fit the signal and background of the invariant mass distribution, I have used the combination of Gauss function and a polynomial function. For K_s^0 I have used the function:

$$a \cdot e^{-\frac{(x-b)^2}{2c^2}} + c \cdot x + d \tag{7.1}$$

For Λ I have used the function:

$$a \cdot e^{-\frac{(x-b)^2}{2c^2}} + c \cdot x + d + e \cdot x^2 \tag{7.2}$$

The corresponding fits of invariant mass distribution can be seen in Figure 7.3 and Figure 7.4.

This method seems sufficient for the background close to peaks, but is not very precise for the peak shapes. The fit of the peak was problematic especially at high values of p_T. Therefore, this fit was used only for approximation of peak position and width. To calculate the peak area more precisely, I have used the bin-by-bin counting method. I have subtracted the fitted polynomial background bin-by-bin and then calculated the peak areas bin-by-bin. The results, uncorrected yields of K_s^0 and Λ as a function of V0 transverse momentum can be seen in Figure 7.5.

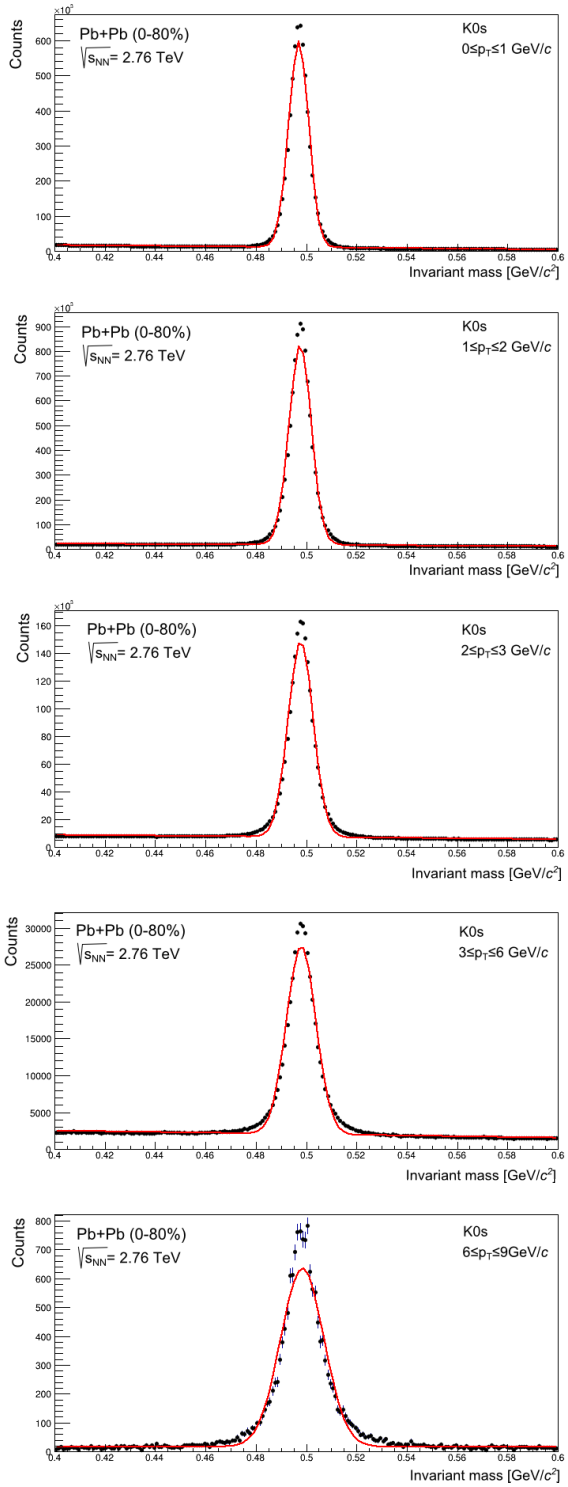

Figure 7.3: Invariant mass spectra of K_s^0 for various intervals of V0 p_T from the ALICE PbPb collisions $\sqrt{s_{NN}}$ =2.76 TeV.

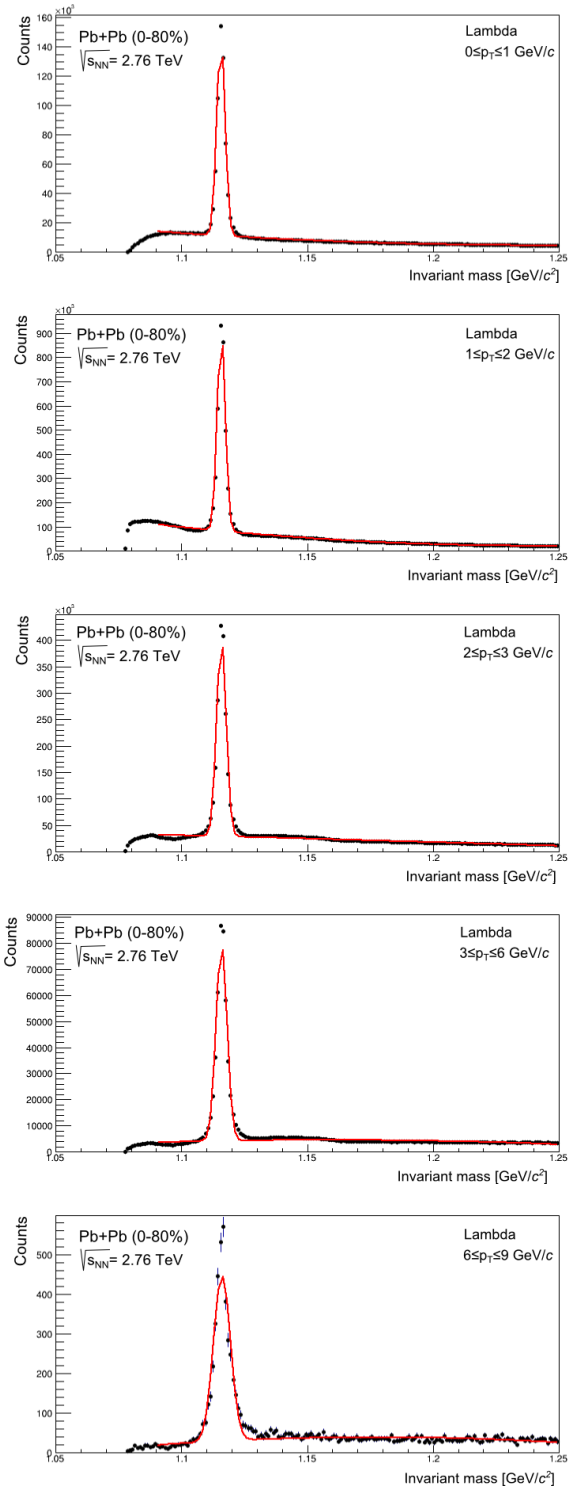

Figure 7.4: Invariant mass spectra of Λ for various intervals of V0 p_T from the ALICE PbPb collisions $\sqrt{s_{NN}}$ =2.76 TeV.

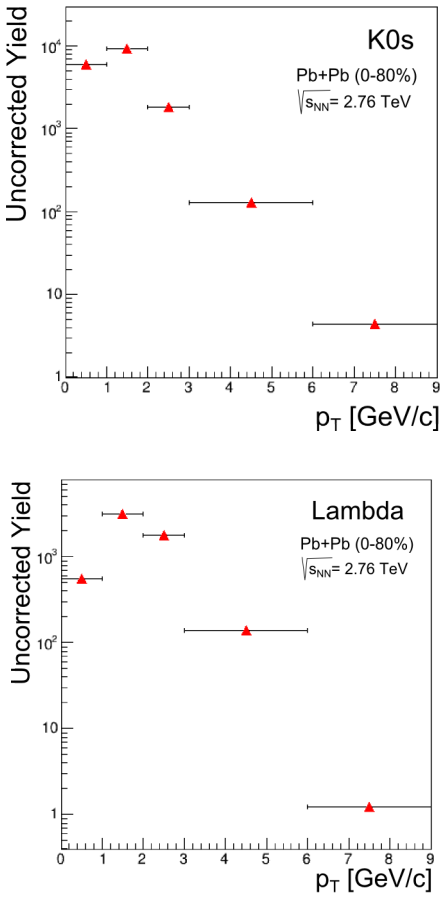

Figure 7.5: Analysis results: uncorrected K_s^0 and Λ yield as a function of V0 transverse momentum from the ALICE PbPb collisions $\sqrt{s_{NN}}$ =2.76 TeV received by bin-by-bin counting method.

Summary

This work was a preparation for further analysis of jets in heavy-ion collisions in the ALICE experiment.

A few microseconds after the Big Bang, the universe is predicted to be in the extremely hot and dense state, referred to as quark-gluon plasma. The theoretical background of quark-gluon plasma, namely standard model and quantum chromodynamics, was briefly described in this thesis.

The extreme conditions for creating of quark-gluon plasma, can be reached in laboratory, in high energy nucleus-nucleus collisions. Basic characteristics of such collision, namely geometry and space time evolution, were discussed.

As the quark-gluon plasma occurs only in the early stage of a collision, and immediately converts to a hadronic matter, it cannot be directly observed. However, there are several indirect observables considered as probes of quark-gluon plasma. The most promising fields of research, including measurement of jet modifications, were summarised. Important results from two experiments, ALICE and STAR, were also mentioned.

Jet reconstruction is the main topic of this thesis. The important jet characteristics were described. Jet algorithms were discussed in detail and compared. Jet areas and their use for background subtraction were also presented. Basic principle of exploring the jet structure was mentioned.

A brief summary of important experiments, with further insight to the ALICE experiment at LHC at CERN, was also discussed in this thesis.

Finally, the principle of topological reconstruction of strange particles in jets with analysis of uncorrected K^0_s and Λ yields from PbPb $\sqrt{s_{NN}}$=2.76 TeV data from the ALICE experiment was presented.

Appendices

Appendix A

Collision kinematic and dynamic variables

Before concentrating on important characteristics of a collision, it is necessary to define observables, that can describe the collision. In a collider, particles, such as electrons or protons, are accelerated at very high, mostly ultrarelativistic (v$\tilde{c}$), velocities and then they collide with each other.

As there are ultrarelativistic velocities in heavy-ion experiment, it is necessary to discuss Lorenz transformations of all observables. To describe observables of a nucleus-nucleus collision, it is useful to define additive and Lorenz invariant variables. They are all schematically shown in Figure A.1.

Let $P = (E, p_x, p_y, p_z)$ be the 4-momentum of a particle. The value of $\vec{p}$ $p = \sqrt{p_x^2 + p_y^2 + p_z^2}$ part can be divided to:

- Longitudinal momentum

$$p_{||} = p_z \tag{A.1}$$

- Transverse momentum

$$p_T = \sqrt{p_x^2 + p_y^2} = p \sin\theta \tag{A.2}$$

The relativistic invariant variable for a momentum is transverse momentum. Instead of longitudinal momentum, relativistic invariant variable called rapidity is used[2]. The rapidity is defined as:

$$y = \frac{1}{2} \ln \frac{E + p_z}{E - p_z} \tag{A.3}$$

To determine rapidity of a particle, it is necessary to measure its E and p_z. Because in many experiments, it is much easier, or even only possible to measure the angle between particle momentum and beam axis $\theta = \arccos \frac{p_z}{p}$, it is useful to define a new variable, pseudorapidity, as [2]

$$\eta = -\ln\left(\tan\frac{\theta}{2}\right) \tag{A.4}$$

The higher is the value of rapidity, that a detector can measure, the larger angle of particles can the detector catch. However, in every detector, some part of signal is lost in the beam direction.

Another commonly used variable is the transverse mass [2]

$$m_T = \sqrt{p_T^2 + m^2} \tag{A.5}$$

where m is the rest mass of the measured particle.

In the collision of two nuclei with atomic and proton numbers (A_1, Z_1) and (A_2, Z_2) , with momentum per the beam p^p (per unit of $\frac{Z}{A}$), the centre of mass energy per nucleon- nucleon pair is defined as [22]

$$\sqrt{s} = \sqrt{(E_1 + E_2)^2 - (\vec{p_1} + \vec{p_2})^2} \simeq \sqrt{4 p_1 p_2} = 2\sqrt{\frac{Z_1 Z_2}{A_1 A_2} p^p} \tag{A.6}$$

The signal of an outgoing particle is provided in the lognitudial and azimuthal space of a detector, namely in $\theta - \phi$ space. Measured values of p_T are often represented by a point in $\eta - \phi$ space. ϕ is the azimuthal angle $\phi = \arctan \frac{p_y}{p_x}$. In this space, particles travelling from the collision region lie near each other.

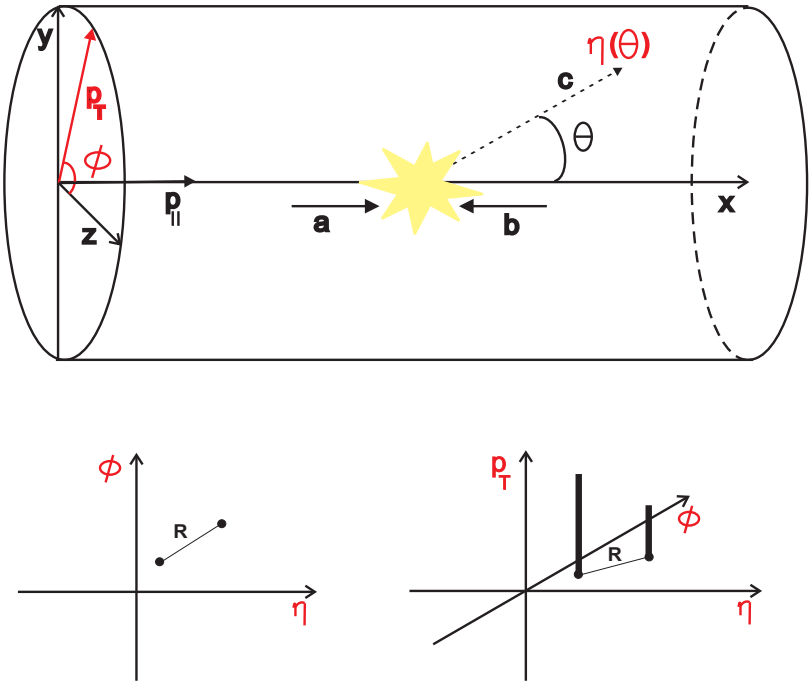

Figure A.1: Collision kinematics variables. Observed particles in η-ϕ space

Appendix B

Glauber model

The number of interacting nucleons in a nucleus-nucleus collision can be characterized by a Glauber model[4]. In this model, nucleus-nucleus collisions are treated as multiple nucleon-nucleon interactions. There are following assumptions taken into account:

- Nucleons travel in straight lines
- Nucleons are not deflected after the collisions
- There is no secondary particle production and excitation of nucleons (nucleon-nucleon inelastic cross section σ_{NN}^{in} is the same as in the vacuum.)

Glauber model is a good aproximation at very high energies. The geometry of Glauber model is shown in Figure B.1. In a collision with an impact parameter b, the number of paticipants N_{part} and number of all binary nucleon-nucleon collisions N_{binary}, respectively, are defined as follows:

$$N_{part}(b) = \int d^2\vec{s} T_A(\vec{s}) \left(1 - e^{(-\sigma_{NN}^{in} T_B(\vec{s})}\right) + \int d^2\vec{s} T_B(\vec{s} - \vec{b}) \left(1 - e^{(-\sigma_{NN}^{in} T_A(\vec{s})}\right) \tag{B.1}$$

$$N_{binary}(b) = \int d^2\vec{s} \sigma_{NN}^{in} T_A(\vec{s}) T_B(\vec{s} - \vec{b}), \tag{B.2}$$

where T_A is the nuclear overlap function, defined as:

$$T_A(\vec{s}) = \int dz \rho_A(z, \vec{s}), \tag{B.3}$$

where ρ_A is the nuclear mass number density normalized to mass number A.

The average number of participants is $N_{part} = 2$ for pp collisions, $N_{part} = N_{binary} + 1$ for Ap collisions and about $N_{part} = 2A$ for central AA collisions. [22]

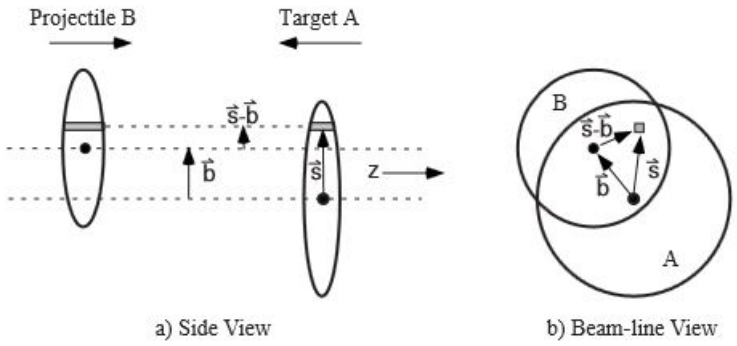

Figure B.1: Glauber model geometry in side and beam-line view. Taken from [6]

Appendix C

Particle identification techniques

Particle identification detectors use different techniques to identify particles. The energy loss per unith path length and time of flight measurement will be discussed in following paragraphs.

C.1 Energy loss per unit path length

The energy loss per unit path length is described by the Bethe- Bloch formula:

$$\left\langle -\frac{dE}{dx} \right\rangle = 2\pi N_a r_e^2 mc^2 \rho \frac{Z}{A} \frac{z^2}{\beta^2} \left[\ln(\frac{2mc^2\gamma^2\beta^2 W_{max}}{I^2}) - 2\beta^2 - \delta - 2\frac{C}{Z} \right] \quad \text{(C.1)}$$

Where m_e is the electron mass, r_e is classical electron radius, Z the charge number of the medium, A is atomic mass of medium, z is charge number of the incident particle, W_{max} is maximum energy transfer in a single collision, e the elementary charge, β the velocity of the particle, I the mean excitation energy of the atom and δ is the density correction. The energy loss curve is drawn in Figure C.1. The point of minimum energy loss is reffered to as *minimum ionisation*. It is followed by a relativistic rise region.

C.2 Time of flight

The time of flight measurement is based on the measured time difference between two parts of a detector. The velocity of a particle is calculated as:

$$\beta = \frac{s}{c\Delta t} \quad \text{(C.2)}$$

With momentum of a particle known (from the $\frac{dE}{dx}$ measurement), the mass of a particle can be calculated as:

$$m = p\sqrt{\frac{1}{\beta^2} - 1} \quad \text{(C.3)}$$

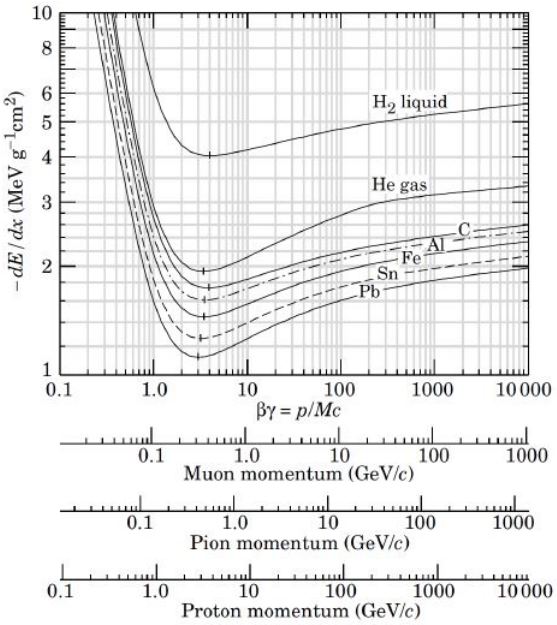

Figure C.1: Energy loss per unit path length for various materials. Taken from [44]

Bibliography

[1] Wikimedia Commons. The standard model of elementary particles. http://en.wikipedia.org/wiki/File:Standard_Model_of_Elementary_Particles.svg, 2013. [online30. 1. 2013].

[2] C.Y. Wong. *Introduction to high-energy heavy ion collisions.* World Scientific, 1995.

[3] David Griffiths. *Introduction to Elementary Particles.* Wiley-VCH, 2008.

[4] K. Yagi, T. Hatsuda, and Y. Miake. *Quark-gluon plasma: From big bang to little bang.* Cambridge University Press, 2005.

[5] Robert Craig Group. Measurement of the inclusive jet cross section using the midpoint algorithm in Run II at CDF. 2006.

[6] Michael L. Miller, Klaus Reygers, Stephen J. Sanders, and Peter Steinberg. Glauber modeling in high energy nuclear collisions. *Ann.Rev.Nucl.Part.Sci.*, 57:205–243, 2007.

[7] Sarah-Louise Blyth. Jet Study in Ultra-Relativistic Heavy-Ion Collisions with the ALICE Detectors at the LHC. 2006.

[8] In-Kwon Yoo. High-energy heavy-ion collisions. http://him.phys.pusan.ac.kr/~yoo/html/PHDhtml/node6.html, 2001. [online15. 5. 2013].

[9] D.D. Chinellato. Strange and Multi-Strange Particle Production in ALICE. 2012.

[10] K Aamodt et al. Elliptic flow of charged particles in Pb-Pb collisions at 2.76 TeV. *Phys.Rev.Lett.*, 105:252302, 2010.

[11] Probing the perfect liquid with the star grid. http://www.interactions.org/sgtw/2006/1025/star_grid_more.html, 2001. [online30. 5. 2013].

[12] Agnes Mocsy and Peter Petreczky. Color screening melts quarkonium. *Phys.Rev.Lett.*, 99:211602, 2007.

[13] J. Adams et al. Evidence from d + Au measurements for final state suppression of high p(T) hadrons in Au+Au collisions at RHIC. *Phys.Rev.Lett.*, 91:072304, 2003.

[14] Stephen Horvat. Charged Hadron Nuclear Modification Factors in the Beam Energy Scan data from STAR. http://drupal.star.bnl.gov/STAR/files/cpod2013HorvatFinal_0.pptx. [online2. 5. 2013] .

[15] K. Aamodt et al. Suppression of Charged Particle Production at Large Transverse Momentum in Central Pb–Pb Collisions at $\sqrt{s_{NN}} = 2.76$ TeV. *Phys.Lett.*, B696:30–39, 2011.

[16] Christine Nattrass. *System, energy, and flavor dependence of jets through di-hadron correlations in heavy ion collisions*. PhD thesis, Yale university, 2009.

[17] Helen Caines. Jets and jet-like correlations studies from STAR. *J.Phys.*, G38:124019, 2011.

[18] Matteo Cacciari and Gavin P. Salam. Jet clustering in particle physics, via a dynamic nearest neighbour graph implemented with CGAL. 2006.

[19] Gerald C. Blazey, Jay R. Dittmann, Stephen D. Ellis, V. Daniel Elvira, K. Frame, et al. Run II jet physics. pages 47–77, 2000.

[20] Rick D. Field. The Underlying event in hard scattering processes. *eConf*, C010630:P501, 2001.

[21] Jessie Shelton. TASI Lectures on Jet Substructure. 2013.

[22] Constantinos A. Loizides. Jet physics in ALICE. 2005.

[23] Gavin P. Salam. Towards Jetography. *Eur.Phys.J.*, C67:637–686, 2010.

[24] Gavin P. Salam and Gregory Soyez. A Practical Seedless Infrared-Safe Cone jet algorithm. *JHEP*, 0705:086, 2007.

[25] Matteo Cacciari, Gavin P. Salam, and Gregory Soyez. The Anti-k(t) jet clustering algorithm. *JHEP*, 0804:063, 2008.

[26] Matteo Cacciari and Gavin P. Salam. Dispelling the N^3 myth for the k_t jet-finder. *Phys.Lett.*, B641:57–61, 2006.

[27] Gregory Soyez. Jet areas as a tool for background subtraction. 2009.

[28] Matteo Cacciari and Gavin P. Salam. Pileup subtraction using jet areas. *Phys.Lett.*, B659:119–126, 2008.

[29] Betty Abelev et al. Measurement of Event Background Fluctuations for Charged Particle Jet Reconstruction in Pb-Pb collisions at $\sqrt{s_{NN}} = 2.76$ TeV. *JHEP*, 1203:053, 2012.

[30] G. Aad et al. Study of Jet Shapes in Inclusive Jet Production in *pp* Collisions at $\sqrt{s} = 7$ TeV using the ATLAS Detector. *Phys.Rev.*, D83:052003, 2011.

[31] Ulrich W. Heinz and Maurice Jacob. Evidence for a new state of matter: An Assessment of the results from the CERN lead beam program. 2000.

[32] Wolfram Fischer. Run overview of rhic. `http://www.rhichome.bnl.gov/RHIC/Runs/`, 2013. [online20. 5. 2013].

[33] Itzhak Tserruya. The Strongly Interacting Quark Gluon Plasma at RHIC and LHC. 2012.

[34] Bastian Bathen. *Jet Measurements and Reconstruction Biases in Proton-Proton and PbPb Collisions with ALICE at the LHC.* PhD thesis, WWU Munster, 2012.

[35] G Alessandro et al. ALICE: Physics performance report, volume II. *J.Phys.*, G32:1295–2040, 2006.

[36] F Carminati et al. ALICE: Physics performance report, volume I. *J.Phys.*, G30:1517–1763, 2004.

[37] Vittorio Frigo. Alice detector. AC Collection. Legacy of AC. Pictures from 1992 to 2002., Mar 1997.

[38] Marek Chojnacki. *Measurement of pions, kaons and protons with the ALICE detector in pp collisions at the LHC.* PhD thesis, Utrecht University, 2012.

[39] Plamen Rumenov Petrov, Orlando Villalobos Baillie, and Peter G Jones. *Strangeness enhancement in high multiplicity proton-proton collisions at* $\sqrt{s} = 7$ *TeV with the ALICE detector at the LHC.* PhD thesis, Birmingham U., 2012. Presented 08 Feb 2013.

[40] K. Aamodt et al. Strange particle production in proton-proton collisions at sqrt(s) = 0.9 TeV with ALICE at the LHC. *Eur.Phys.J.*, C71:1594, 2011.

[41] K. Aamodt et al. The ALICE experiment at the CERN LHC. *JINST*, 3:S08002, 2008.

[42] Chiara Bianchin, Marcello Lunardon, and Andrea Dainese. *Charm production at the LHC via* $D^0; K^-\pi^+$ *reconstruction in ALICE:cross section in pp collisions and first flow measurement in Pb-Pb collisions.* PhD thesis, Padova U., Jan 2012. Presented 21 Mar 2012.

[43] P Cortese et al. Alice electromagnetic calorimeter technical design report. (CERN-LHCC-2008-014. ALICE-TDR-14), Aug 2008.

[44] W.-M. Yao et al. Review of Particle Physics. *Journal of Physics G*, 2006.